JOURNAL OF MOLECULAR LIQUIDS

ISSN: 0167-7322

PUBLISHER ELSEVIER

Impact Factor: 4.513

Accepted November 30th 2018

SUPERCRITICAL HEAT TRANSFER CHARACTERISTICS OF COUPLE STRESS CONVECTION FLOW FROM A VERTICAL CYLINDER USING AN EQUATION OF STATE APPROACH

Hussain Basha[1], G. Janardhana Reddy[1*], N. S. Venkata Narayanan[2] and **O. Anwar Bég[3]**

[1]Department of Mathematics, Central University of Karnataka, Kalaburagi, India-585367
[2]Department of Chemistry, Central University of Karnataka, Kalaburagi, India-585367
[3]Fluid Mechanics, Aeronautical and Mechanical Engineering Department, School of Computing, Science and Engineering, University of Salford, Manchester M54WT, UK

[*]Corresponding author-Email: gjr@cuk.ac.in

ABSTRACT

The present work describes numerical simulations of the supercritical heat transfer characteristics of couple stress fluid flow from a vertical cylinder using the equation of state approach. Redlich-Kwong (RK-EOS) and Van der Waals (VW-EOS) equations of state (EOS) are deployed to derive the equation for the thermal expansion coefficient (β). The β values calculated based on RK-EOS are sufficiently close to the experimental values when compared with those based on VW-EOS. Due to the presence of couple stresses in the fluid, highly nonlinear coupled partial differential equations are generated. These primitive equations are reduced to dimensionless form by using suitable non-dimensional quantities. An unconditionally stable finite difference technique is used to solve the normalized conservation equations under physically viable boundary conditions, in order to describe the natural convection heat transfer characteristics of couple stress fluid external to a vertical cylinder in the supercritical region. For different values of the emerging physical parameters, numerical data for couple stress fluid for the case of Nitrogen is generated and presented in the form of graphs and tables. The present computations indicate that the velocity field is suppressed close to the cylinder whereas it is enhanced away from the cylinder with increasing values of reduced temperature in the supercritical fluid region. The reverse behavior is observed for reduced pressure. The present results are compared with the previous results and found to be in good agreement. Applications of the model include super-critical coating dynamics in the aerospace and medical industries.

KEYWORDS: *Supercritical Couple Stress Fluid, Heat transfer, RK-EOS, Nitrogen, Compressibility Factor, Reduced Temperature, Crank-Nicolson method, Cylinder coating.*

NOMENCLATURE

$C_f, \overline{C_f}$	local and average wall shear stress
C_p	specific heat capacity

d	diameter of cylinder
d_{ij}	tensor corresponding to deformation rate
g	gravitational field
Gr	free convection parameter
H^*	dimensional heat function
H	dimensionless heat function
i, j	corresponding to mesh points along (X, R) directions
k	thermal conductivity
m_{ij}	couple stress tensor
m	trace of couple stress tensor
$Nu_X, \overline{Nu}$	local and average heat transfer rate
P	pressure
Pr	Prandtl number
P_r^*	dimensional reduced pressure
r	radial axis
R	dimensionless radial axis
r_o	radius of cylinder
Ra_X	local Rayleigh number
T_r^*	dimensional reduced temperature
t'	time
t	non-dimensional time
T'	temperature
$\boldsymbol{U}$	velocity vector
u, v	components of velocity along x, r directions
U, V	components of dimensionless velocity along X, R directions

x	coordinate along axial direction
X	dimensionless axial coordinate
Z	compressibility factor

Greek letters

α	thermal diffusivity
β	volumetric thermal expansion coefficient
δ_{ij}	Kronecker delta
ε_{ijk}	Levi-Civita symbol
τ_{ij}	force stress tensor
η, η'	viscosity coefficients of couple stress fluid
θ	non-dimensional temperature
ρ	density of the fluid
ψ	stream function
μ, λ	fluid viscosity coefficients
ν	kinematic viscosity
ω	vector corresponds to spin
ω_{ij}	tensor corresponds to spin

Subscripts

c	critical condition
r	reduced characteristics
w	conditions defined at wall
∞	conditions defined far away from the wall

Superscripts

k	time step level

1. INTRODUCTION

It is evident from the available literature that, presently, many scientists and engineers are studying the physical and chemical properties of non-Newtonian fluid flows in different geometries due to their widespread industrial and technological applications. These applications include the manufacture of cosmetic and food products, polymer fluids extrusion, liquid crystals solidification, exotic lubricants, coating with smart materials, drilling muds, bio-technological suspension synthesis etc. Although a rich spectrum of mathematical models have been developed for non-Newtonian behavior, most of these models (e.g. viscoelastic, viscoplastic, power-law etc) neglect *micro-structural* features. The *couple stress* fluid model however allows for the simulation of micro-structural phenomena and has therefore attracted the curiosity of many authors. The molecular spin in couple stress fluids generates anti-symmetric stresses, which produce interesting hydrodynamic and thermodynamic behavior as compared with Newtonian or alternate non-Newtonian models. A very important characteristic of couple stress fluid is that, the stress tensor is not symmetric and hence the classical Newtonian fluid flow model fails to predict its exact flow behavior in practical systems. Thus, to overcome this difficulty Stokes [1] generalized the classical viscous fluid flow model by accounting body couples and couple stresses in the governing equations. The fundamental thermodynamics and constitutive equations for couple stress fluids have been lucidly elaborated also by Stokes [2]. With regard to the other so-called “polar fluid theories” the couple stress fluid theory features both the classical Cauchy stresses along with supplementary couple stresses in the fluid. However, it is clear from the literature [2] that couple stress fluids contains *rigid and randomly oriented fluid particles* suspended in a viscous fluid medium. Couple stress fluids are therefore a robust approximation for industrial and biological liquids featuring randomly oriented and inflexible (non-deformable) fluid particles suspended in viscous medium and good examples include blood, synthetic fluids, sedimentary suspensions,

liquid crystals, electro-rheological fluids, synovial fluids, lubricants with polymer additives, certain solar gel paints and colloidal fluids.

Largely due to the elegance and simplicity of the Stokes' couple stress model, Stokes' couple stress fluid theory [1, 2] has been employed extensively in a number of problems of relevance to industrial applications particularly in lubrication theory [3-8]. In addition to this couple stress fluid theory has found considerable applications in bio-fluid mechanics and bio-engineering. Non-Newtonian effects in hemodynamics become important in small blood vessels where the standard Newtonian theory fails to capture the behavior of cell aggregation, viscosity modifications, erythrocyte tumbling etc. Valanis and Sun [9] successfully applied the couple stress fluid theory to predict the rheological behavior and thermodynamic properties of blood in Poiseuille flow. Srivastava [10] simulated peristaltic blood flow using couple stress fluid theory. Branching arterial blood flow was investigated by Agrawal and Anwaruddin [11]. Further, Srivastava [12] used the couple stress fluid model to examine the influence of mild stenosis on blood flow in vessels. Maiti and Misra [13] theoretically investigated the peristaltic transport characteristics of a couple stress fluid in a porous channel. Further, in their study the behavior of physiological flow of blood in the micro-circulatory system is investigated by accounting of the particle size effect. Murthy *et al.* [14] studied entropy generation with radiative heat transfer in couple stress fluids with applications in nuclear engineering cooling systems. More recently couple stress fluid theory has been deployed in embryological transport [15], micro-electro-osmotic pumps [16], chemically-reacting thermo-solutal coating flows [17] and gastric magnetic therapy [18].

Modern biomedicine faces increasing challenges related to infections, atherosclerosis, mitral stenosis, angina pectoris, arrhythmia and dysrhythmia, cardiac ischemia, heart failure, stroke, peripheral artery disease (PAD) and venous thromboembolism (VTE) etc. It is very difficult to control all these physiological problems by using conventional drugs and

technologies. Modern pharmaceutical and chemical industries require continuous development of innovative new drugs for various diseases and require improvement of the curative drug efficiency against various pathologies. Simultaneously a constant effort is underway to move towards environment-friendly chemical, biological and industrial process and considerably reduce the use of toxic and potentially harmful solvents. Another objective in modern times is to enhance the energy efficiency and transition to more sustainable and green economies and significantly reduce environmental pollution. Therefore, to overcome all these difficulties as mentioned and discussed above, the concept of supercritical fluid (SCF) is being increasingly explored in the pharmaceutical, chemical (chromatographic and extraction processes), energy and other industries in large scale production of for example new and efficient drugs, more robust (smart) coatings for engineering devices, thermal process enhancement etc. Supercritical fluids are usually treated as green solvents and are therefore excellent candidates for achieving alternate green technologies across a range of engineering sectors. Supercritical fluids (SCF's) refer to substances (gases or liquids) having their temperature and pressure above the thermodynamic critical point. In the vicinity of the critical point, liquids as well as gases are in the *same phase*. It is clear from the experimental and theoretical studies that, the chemical and physical properties of SCF's are completely different from those of common fluids like gases and liquids and they are unique in nature. In other words, SCF's had the properties of both liquids as well as gases at their supercritical state and these properties are tunable and have large number advantages in industrial systems. Moreover, supercritical solvents are free from toxic materials and are harmless substances. Supercritical fluids are becoming more popular in modern chromatographic industries, preparation of drugs and bio-active materials, solvent extraction, fractionation, particle design, micro-encapsulation, cell-lysis, pollution abatement, preparation of nano-materials, impregnation, supercritical anti-solvents precipitation (SASP), plasticization of polymers, formation of microcellular foams, microcellular blow moulding,

paints and coatings, ceramics and carbons manufacture, polymer processing, formation of aerogels, dyeing, cleaning, sterilization, and virus inactivation etc. An exhaustive literature about the applications and properties of SCF's can be found in [19-28].

In view of the above discussion, it is evident that to better understand the thermodynamic behavior of fluids at supercritical state, the phenomena of heat transfer in SCF dynamics plays an important role. Thermofluid mechanics constitutes an important area for SCF analysis [29]. Manufacturing coating dynamics of cylinders for example is an important area in the medical and aerospace industries which can benefit from SCF implementation since this geometry features in regenerative cooling in rocket chambers, propulsion ducts, medical pumps, drugs etc. Among various researchers, Sparrow and Gregg [30] thermodynamically investigated the free convection heat transfer phenomena over a cylinder and discussed their numerical results in depth with suitable physical explanations. A similar heat transfer study was described by Lee et al. [31] for a slender vertical cylinder by using a power-law variation with different surface temperature. By considering these two particular problems [30, 31] as the basic models, it is of interest to analyze the heat transfer behavior of different fluids in the supercritical region. However, the phenomena of free convection in SCF region is somewhat problematic, since the physical and chemical properties of these fluids are completely dependent on pressure and temperature and they demonstrate a drastic change in heat transfer characteristics in the vicinity of the critical point. Thus, to investigate the SCF behavior completely, both experimental as well as theoretical studies [32-35] have been reported with respect to different geometries. In the case of natural convection heat transfer to SCF's, the thermal expansion coefficient (β) plays an important role when compared to the other properties. Furthermore, the thermal expansion coefficient directly depends upon the pressure and temperature, when the common fluids approach their supercritical state. However, in many of the free convection heat transfer problems β is treated as constant [36, 37]. Therefore, the

assumption of constant β produces erroneous results *in the vicinity of the critical point* and *above the critical point*. Thus, to overcome this difficulty many researchers have utilized a variety of experimental, theoretical and computational techniques. Among these approaches, the equation of state (EOS) approach is relatively simple but exceptionally accurate and resolves successfully the particular difficulty associated with thermodynamic property variation near and above the critical point. Rolando [38] was the first to implement the Van der Waals equation of state (VW-EOS) in free convection heat transfer to supercritical fluids over a heated vertical flat plate. From [38] one can clearly remark that, β mainly depends on compressibility factor, temperature and pressure too in the proximity of critical point and above the critical point. Further, Teymourtash et al. [39] improved this model by considering both the Redlich-Kwong equation of state (RK-EOS) along with VW-EOS and showed the viability of Boussinesq's approximation to supercritical fluids. However, Khonakdar and Raveshi [40] proved that, among the available equation of states, RK-EOS is a more appropriate and accurate model to evaluate the thermodynamic properties of different fluids in SCF region. Recently Reddy et al. [41, 42] described numerical studies of heat transfer to isobutane and carbon dioxide in SCF region using RK-EOS.

In order to simulate numerically the heat transfer characteristics of couple stress fluid in the supercritical region, we have used nitrogen as a base compound, since it has large scale industrial applications in medical, energy and aerospace technologies. Supercritical nitrogen is used in the nebulization process, polymer processing, purification of reactive porous materials, and formation of nitrogen-doped carbon-based aerogels. However, in the field of biomedicine nitrogen is used to preserve sperm, egg, nerves, blood, stem cells, and various other biological specimens as well as viruses for vaccination. Supercritical nitrogen also features in cryogenic rocket propellants [43]. More detailed literature related to industrial and biomedical applications of nitrogen can found in [44-46].

Further an extensive range of application-oriented studies on supercritical fluids have been presented by a number of researchers. An experimental study of the transition of liquid water to its supercritical state was made by Gorbaty and Bondarenko [47]. From their experimental analysis it is observed that, the probability of hydrogen bonding among water molecules approaches the percolation threshold in the vicinity of the critical temperature. This fact illustrates that an infinite cluster of hydrogen bonded molecules cannot exist in supercritical water, although the probability of hydrogen bonding is still high. Chopra and Choudhury [48] investigated the characteristics of aqueous solution of uranyl ions at the supercritical state by utilizing molecular dynamics simulations, also considering the effects of water density on hydrogen structure. Solovieva et al. [49] used the supercritical fluid impregnation method to study the long-lived colored forms of indoline spirooxazine molecules under their SCF matrix immobilization in polymers. The behavior of solubility parameter associated with supercritical CO_2 in the extraction process was studied by Zhang et al. [50] using a molecular dynamics simulation method and it was found that the solubility parameter increases with increasing pressure and diminishes with magnifying temperature. Artemenko et al. [51] made an attempt to study the boundary between the gas and liquid phases beyond the thermodynamic critical point. Their investigation showed that only a single Widom line lies almost on the critical isochore. Recently, Bagheri et al. [52] investigated the Rapid Expansion of Supercritical Solutions (RESS) process by considering the four different binary solid drug-supercritical solvent systems such as Ibuprofen-CO_2, Aspirin-CO_2, Salicylic acid-CO_2 and Griseofulvin-CHF_3. They employed a cubic equation of state and mixing rules to analyze the considered problem. The molecular dynamics and transport properties of supercritical carbon dioxide were investigated by Mohammed and Mansoori [53] using a molecular dynamics simulation method. Their study reports that, the solubility of carbon dioxide is low in brine and high crude oil. Further, Yadav [54] studied the vibrational spectral diffusion process and

associated structural and dynamical properties of ammonia in the supercritical state using a molecular dynamics simulation method. This study indicated that the hydrogen bond between ammonia molecules diminishes considerably as the flow changes from normal liquid state to the supercritical state.

Thus, by considering the above-mentioned applications and advantages of couple stress fluid theory in physiological fluid flows, we have considered the supercritical couple stress fluid for the present numerical simulations. Relatively few studies have been communicated with regard to numerical heat transfer in the supercritical fluid region [38-42]. The current analysis focuses on *unsteady boundary layer flow and free convection in supercritical flow of couple stress fluid over a vertical cylinder.* This problem has not yet been reported in the literature and involves considerable complexity and nonlinearity. Supercritical heat transfer characteristics of the couple stress fluid are modeled with both the robust RK-EOS and VW-EOS approaches. A numerical method (unconditionally stable Crank-Nicolson iteration scheme) is employed to solve the governing transformed non-dimensional conservation equations which are derived based on the laws of fluid motion. In the present thermodynamic study the flow is assumed to be laminar, viscous and incompressible. The obtained numerical results are compared with the available experimental and theoretical results and found to be in good agreement. Extensive visualization of results is provided with detailed elaboration of the thermal physics.

2. EQUATION OF β BASED ON EQUATION OF STATE APPROACH (EOS)

With the help of the equation of state approach, two suitable equations to calculate β are derived. Herein we apply both the RK-EOS and VW-EOS approaches to derive the appropriate equations for β. Thus, $\beta = \frac{1}{T'}\left[1 - \left(\frac{3.5AB+2ZB^2+BZ-2.5AZ}{3Z^3-2Z^2+Z(A-B)-B^2Z}\right)\right]$ and $\beta = \frac{1}{T'}\left[1 - \left(\frac{Z^2B-2ZA+3AB}{3Z^3-2Z^2(B+1)+AZ}\right)\right]$ are the required thermodynamic equations derived using RK-EOS and

VW-EOS models. More detailed explanation about these derivations can be found in the available literature [42]. Here A and B are constants obtained from critical properties and Z is the compressibility factor. The reason for deriving these equations is that in natural convection problems β is assumed to be constant. However, this assumption produces the wrong results in the supercritical fluid region as illustrated in **Fig. 1**. This deviation is, due to the fact that, in the case of free convection heat transfer process, β is assumed to be independent of temperature and pressure. However, in the case of supercritical fluids β is completely dependent on compressibility, pressure and temperature. Thus, to investigate the free convection properties of couple stress fluids in the supercritical region, a more appropriate EOS is essential. Thus, the present article utilizes above mentioned EOS models to derive equations for β in SCF region.

3. MODEL FOR SUPERCRITICAL HEAT TRANSFER FROM A CYLINDER

The present thermodynamic analysis considers the laminar buoyancy-driven free convection heat transfer characteristics of viscous incompressible couple stress fluid flow past vertical a cylinder numerically in SCF region. Figure 1 shows the idealized phase diagram for the SCF (nitrogen) and Fig. 2 corresponds to the flow configuration of the present problem. A suitable rectangular coordinate system is used to describe the current problem. The x-coordinate is measured along the axis of the cylinder and the r-coordinate is taken normal to the x-axis. Initially ($t' = 0$) the temperature of the cylinder and surrounding fluid are supposed to be T'_∞. After some time interval ($t' > 0$), the temperature T'_∞ is elevated to T'_w and maintained at this new value for $t' > 0$. With this temperature difference, in the neighborhood of the hot cylinder, a density difference will arise and via interaction with the gravitational field will produce natural (free) convection in the couple stress flow over the vertical cylinder. For the current problem, Boussinesq's approximation is applicable [39]. Thus, with all the above

considerations, the relevant equations governing the supercritical couple stress convection boundary layer flow over the vertical cylinder [41, 42, 55] are given as follows:

$$\frac{\partial(ru)}{\partial x}+\frac{\partial(rv)}{\partial r}=0 \tag{1}$$

$$\rho\left(\frac{\partial u}{\partial t'}+u\frac{\partial u}{\partial x}+v\frac{\partial u}{\partial r}\right)=\rho g\beta(T'-T'_{\infty})+\frac{\mu}{r}\frac{\partial}{\partial r}\left(r\frac{\partial u}{\partial r}\right)-\eta\nabla^4 u \tag{2}$$

$$\frac{\partial T'}{\partial t'}+u\frac{\partial T'}{\partial x}+v\frac{\partial T'}{\partial r}=\frac{\alpha}{r}\frac{\partial}{\partial r}\left(r\frac{\partial T'}{\partial r}\right) \tag{3}$$

On account of the couple stresses, the biharmonic operator ($\nabla^4=\nabla^2.\nabla^2$) is added in Eq. (2). Further, the couple stress fluid constant η is also featured in Eq. (2). It is clear from couple stress fluid theory [1, 2] that, the ratio of η and μ (dynamic viscosity) has the dimension of l^2 (length square), i.e., $l^2(=\eta/\mu)$ and this ratio is suitably defined based on size of the fluid molecules [5]. Thus, the stress tensors associated with couple stresses in the SCF fluid are defined by Stokes couple stress fluid theory [1, 2] as follows:

$$\tau_{ij}=(-P+\lambda\nabla.\mathbf{U})\delta_{ij}+2\mu d_{ij}-\frac{1}{2}\varepsilon_{ijk}\left(m_{ij}+4\eta\omega_{k,rr}+\rho c_k\right) \tag{4}$$

$$m_{ij}=\frac{1}{3}m\delta_{ij}+4\eta'\omega_{j,i}+4\eta\omega_{i,j} \tag{5}$$

Here $\omega=\frac{1}{2}(\nabla\times\mathbf{U})$, $m=m_{11}+m_{22}+m_{33}$ and $\omega_{k,rr}=\omega_{k,11}+\omega_{k,22}+\omega_{k,33}$. All the symbols are listed in nomenclature section. However, in Eqs. (4) and (5), τ_{ij} denote the stress tensor related to force, m_{ij} indicate the couple stress tensor, $\omega_{i,j}$ designate the tensor related to spin, d_{ij} is rate of deformation tensor, $\boldsymbol{U}$ is velocity vector, P is pressure, δ_{ij} is Kronecker delta operator, ε_{ijk} is the Levi-Civita symbol, ρc_k is body couple vector and ω is spin vector. Further, in the couple stress fluid theory, viscosity coefficients are represented by λ and μ, also the viscosity coefficients associated with couple stresses are denoted by η and η'. These quantities are related to one another by the following inequality relation.

$$\mu \geq 0, 2\mu + 3\lambda \geq 0, \eta \geq 0 \text{ and } |\eta'| \leq \eta \tag{6}$$

In the couple stress fluid theory [1], two main observations are made. Firstly, at the boundary couple stresses disappear. Secondly the rotational velocity of the boundary is equal to the fluid vorticity on the boundary. Among these two conditions, the second boundary condition is appropriate for the present problem $(\text{i.e.} \nabla \times \mathbf{U} = 0)$. Based on these assumptions, the appropriate initial and boundary conditions for the present regime are obtained as follows:

$$\left.\begin{array}{ll} t' \leq 0: \; T' = T'_\infty, \; u = 0, \; v = 0 & \forall\, x \text{ and } r \\ t' > 0: \; T' = T'_w, \; u = 0, \; v = 0 & \text{at } r = r_o \\ \quad\;\; T' = T'_\infty, \; u = 0, \; v = 0 & \text{at } x = 0 \\ \quad\;\; T' \to T'_\infty, \; u \to 0, \; v \to 0 & \text{as } r \to \infty \end{array}\right\} \tag{7}$$

and

$$\frac{\partial u}{\partial r} = \frac{\partial v}{\partial x} \text{ at } r = r_o \text{ and as } r \to \infty \tag{8}$$

Invoking the following non-dimensional parameters:

$$\left.\begin{array}{c} X = Gr^{\frac{-11}{12}} \frac{x}{r_o}, \;\; R = \frac{r}{r_o}, \;\; U = Gr^{\frac{-11}{12}} \frac{ur_o}{\nu} \\ V = \frac{vr_o}{\nu}, \quad t = \frac{\nu t'}{{r_o}^2}, \;\; \theta = \frac{T' - T'_\infty}{T'_w - T'_\infty} \\ Gr = \frac{g\beta r_o^3 (T'_w - T'_\infty)}{\nu^2}, \;\; Pr = \frac{\nu}{\alpha}, \;\; r_o = \left(\frac{\eta}{\mu}\right)^{\frac{1}{2}} \end{array}\right\} \tag{9}$$

Implementation of Eqn. (9) in Eqns. (1)-(3) and (7)-(8), leads to the following reduced non-dimensional conservation equations for mass, momentum and energy (heat):

$$\frac{\partial U}{\partial X} + \frac{\partial V}{\partial R} + \frac{V}{R} = 0 \tag{10}$$

$$\frac{\partial U}{\partial t} + U\frac{\partial U}{\partial X} + V\frac{\partial U}{\partial R} = Gr^{1/12}\,\theta + \left(\frac{\partial^2 U}{\partial R^2} + \frac{1}{R}\frac{\partial U}{\partial R}\right) - \left(\frac{1}{R^3}\frac{\partial U}{\partial R} - \frac{1}{R^2}\frac{\partial^2 U}{\partial R^2} + \frac{2}{R}\frac{\partial^3 U}{\partial R^3} + \frac{\partial^4 U}{\partial R^4}\right) \tag{11}$$

$$\frac{\partial \theta}{\partial t} + U\frac{\partial \theta}{\partial X} + V\frac{\partial \theta}{\partial R} = \frac{1}{Pr}\left(\frac{\partial^2 \theta}{\partial R^2} + \frac{1}{R}\frac{\partial \theta}{\partial R}\right) \tag{12}$$

The normalized boundary conditions emerge as:

$$\left.\begin{array}{rl} t \le 0 : \theta = 0, & U = 0,\ V = 0 \quad \forall\, X \text{ and } R \\ t > 0 : \theta = 1, & U = 0,\ V = 0 \quad \text{at } R = 1 \\ \theta = 0, & U = 0,\ V = 0 \quad \text{at } X = 0 \\ \theta \to 0, & U \to 0,\ V \to 0 \quad \text{as } R \to \infty \end{array}\right\} \tag{13}$$

and

$$\frac{\partial U}{\partial R} = \frac{1}{Gr^2}\frac{\partial V}{\partial X} \text{ at } R = 1 \text{ and as } R \to \infty \tag{14}$$

The physical model which is considered in this study has a number of diverse applications in several areas of technology including rocket propulsion trans/super critical-cooling, supercritical fluid extraction industries, nuclear reactors, solar collectors, coating dynamics of aerospace components, green technology, cryogenic containers, refrigeration (suspension of glass beakers), electronic equipment, etc.

4. NUMERICAL SOLUTIONS

The emerging physico-mathematical model defined by Eqns. (10)-(12) with appropriate initial and boundary conditions (13, 14) constitutes a system of highly nonlinear coupled partial differential equations. There are no analytical or direct methods available to solve these coupled equations. Recourse must be made to a computational methodology. The fast converging, numerically stable Crank-Nicolson implicit technique is implemented to solve the transient coupled nonlinear Eqns. (10)-(12) with initial and boundary conditions (13, 14). The Eqns. (10)-(12) are written in their finite difference forms as follows:

$$\frac{U_{i,j}^{k+1} - U_{i-1,j}^{k+1} + U_{i,j}^{k} - U_{i-1,j}^{k}}{2\Delta X} + \frac{V_{i,j}^{k+1} - V_{i,j-1}^{k+1} + V_{i,j}^{k} - V_{i,j-1}^{k}}{2\Delta R} + \frac{V_{i,j}^{k+1}}{(1+(j-1)\Delta R)} = 0 \tag{15}$$

$$\frac{U_{i,j}^{k+1} - U_{i,j}^{k}}{\Delta t} + U_{i,j}^{k}\left(\frac{U_{i,j}^{k+1} - U_{i-1,j}^{k+1} + U_{i,j}^{k} - U_{i-1,j}^{k}}{2\Delta X}\right) + V_{i,j}^{k}\left(\frac{U_{i,j+1}^{k+1} - U_{i,j-1}^{k+1} + U_{i,j+1}^{k} - U_{i,j-1}^{k}}{4\Delta R}\right) = Gr^{1/12}\left(\frac{\theta_{i,j}^{k+1} + \theta_{i,j}^{k}}{2}\right) +$$

$$\left(\frac{U_{i,j+1}^{k+1} - U_{i,j-1}^{k+1} + U_{i,j+1}^{k} - U_{i,j-1}^{k}}{4(1+(j-1)\Delta R)\Delta R}\right) + \left(\frac{U_{i,j-l}^{k+1} - 2U_{i,j}^{k+1} + U_{i,j+1}^{k+1} + U_{i,j-1}^{k} - 2U_{i,j}^{k} + U_{i,j+1}^{k}}{2(\Delta R)^2}\right) - \left(\frac{U_{i,j+1}^{k+1} - U_{i,j-1}^{k+1} + U_{i,j+1}^{k} - U_{i,j-1}^{k}}{4(1+(j-1)\Delta R)^3\Delta R}\right) +$$

$$\left(\frac{U_{i,j-l}^{k+1}-2U_{i,j}^{k+1}+U_{i,j+1}^{k+1}+U_{i,j-1}^{k}-2U_{i,j}^{k}+U_{i,j+1}^{k}}{2(1+(j-1)\Delta R)^2(\Delta R)^2}\right)-\left(\frac{U_{i,j+2}^{k+1}-2U_{i,j+1}^{k+1}+2U_{i,j-1}^{k+1}-U_{i,j-2}^{k+1}+U_{i,j+2}^{k}-2U_{i,j+1}^{k}+2U_{i,j-1}^{k}-U_{i,j-2}^{k}}{2(1+(j-1)\Delta R)(\Delta R)^3}\right)-$$

$$\left(\frac{U_{i,j+2}^{k+1}-4U_{i,j+1}^{k+1}+6U_{i,j}^{k+1}-4U_{i,j-1}^{k+1}+U_{i,j-2}^{k+1}+U_{i,j+2}^{k}-4U_{i,j+1}^{k}+6U_{i,j}^{k}-4U_{i,j-1}^{k}+U_{i,j-2}^{k}}{2(\Delta R)^4}\right) \quad (16)$$

$$\frac{\theta_{i,j}^{k+1}-\theta_{i,j}^{k}}{\Delta t}+U_{i,j}^{k}\left(\frac{\theta_{i,j}^{k+1}-\theta_{i-1,j}^{k+1}+\theta_{i,j}^{k}-\theta_{i-1,j}^{k}}{2\Delta X}\right)+V_{i,j}^{k}\left(\frac{\theta_{i,j+1}^{k+1}-\theta_{i,j-1}^{k+1}+\theta_{i,j+1}^{k}-\theta_{i,j-1}^{k}}{4\Delta R}\right)=$$

$$\left(\frac{\theta_{i,j-1}^{k+1}-2\theta_{i,j}^{k+1}+\theta_{i,j+1}^{k+1}+\theta_{i,j-1}^{k}-2\theta_{i,j}^{k}+\theta_{i,j+1}^{k}}{2Pr(\Delta R)^2}\right)+\left(\frac{\theta_{i,j+1}^{k+1}-\theta_{i,j-1}^{k+1}+\theta_{i,j+1}^{k}-\theta_{i,j-1}^{k}}{4Pr(1+(j-1)\Delta R)\Delta R}\right) \quad (17)$$

Also, the finite difference approximations corresponding to the Eqns. (13) and (14) are as follows:

$$\left.\begin{aligned} t\le 0:\ \theta_{i,j}^{0}=0,\ U_{i,j}^{0}=0,\ V_{i,j}^{0}=0 \quad & \forall\, X \text{ and } R \\ t>0:\ \theta_{i,0}^{k}=1,\ U_{i,0}^{k}=0,\ V_{i,0}^{k}=0 \quad & \text{at } R=1 \\ \theta_{0,j}^{k}=0,\ U_{0,j}^{k}=0,\ V_{0,j}^{k}=0 \quad & \text{at } X=0 \\ \theta_{i,\infty}^{k}\to 0,\ U_{i,\infty}^{k}\to 0,\ V_{i,\infty}^{k}\to 0 \quad & \text{as } R\to\infty \end{aligned}\right\} \quad (18)$$

$$\frac{U_{i,j+1}^{k+1}-U_{i,j-1}^{k+1}+U_{i,j+1}^{k}-U_{i,j-1}^{k}}{4\Delta R}=\frac{V_{i,j}^{k+1}-V_{i-1,j}^{k+1}+V_{i,j}^{k}-V_{i-1,j}^{k}}{2(Gr)^2\Delta X} \quad (19)$$

To obtain the suitable non-dimensional thermodynamic solution which is valid over the non-dimensional time (t), corresponding to Eqns. (10)-(12) with (13) and (14), a suitable solution domain is designed in such a way that, it consists of $X_{min}=0$, $X_{max}=1$, $R_{min}=1$ and $R_{max}=20$, where R_{max} is linked to $R=\infty$ and which is away from boundary layers. Mesh independence test is executed in order to achieve a consistent grid scheme and correct converged solutions, as shown in **Table 1**. The 100X500 grid system is adopted with step sizes 0.03 and 0.01 in R and X directions. **Table 2** illustrates the time-independence test with $\Delta t=0.01$ in the t-direction. The numerical procedure first solves Eqn. (12), by which temperature field is eventually calculated. Similarly, velocity field is obtained by solving the Eqns. (10)-(11), respectively. The recurrence relation at the (k+1)th iteration for the energy Eqn. (12) is governed by a *tridiagonal* equation of the following form:

$$a_{i,j}\,\Gamma_{i,j-1}^{k+1}+b_{i,j}\,\Gamma_{i,j}^{k+1}+c_{i,j}\,\Gamma_{i,j+1}^{k+1}=d_{i,j} \quad (20)$$

Similarly, the velocity Eqn. (11) at the $(k+1)^{th}$ iteration, is governed by a *penta-diagonal* recurrence relation of the form:

$$A_{i,j}\,\Pi_{i,j-2}^{k+1} + B_{i,j}\,\Pi_{i,j-1}^{k+1} + C_{i,j}\,\Pi_{i,j}^{k+1} + D_{i,j}\,\Pi_{i,j+1}^{k+1} + E_{i,j}\,\Pi_{i,j+2}^{k+1} = F_{i,j} \quad (21)$$

Here the symbols Γ and Π denote the transient variables θ and U, respectively. The Eqns. (20) and (21) generate a system of tridiagonal and penta-diagonal equations at every grid point on particular i-level. Thus, the thermodynamic solution of these temperature and velocity equations is obtained by using standard numerical algorithms namely the Thomas algorithm [56] and a penta-diagonal algorithm [57]. Velocity field can also be calculated using the continuity Eqn. (15). To produce numerically stable and accurate results over non-dimensional time (t), the above iteration process is repeated until convergence criteria 10^{-5} is satisfied. In the present numerical scheme, the local truncation error $O(\Delta t^2 + \Delta R^2 + \Delta X)$ approaches zero when $\Delta t \to 0$, $\Delta R \to 0$ and $\Delta X \to 0$ [58]. Thus, it is concluded that, the numerical method which is used in the present simulations is unconditionally stable and hence produces economically reliable results in the supercritical fluid region over non-dimensional time (t). More detailed literature about this numerical method is available in [59, 60].

5. DISCUSSION OF NUMERICAL RESULTS

5.1. Accuracy of RK-EOS

Table 3 documents the necessary thermodynamic critical values related to nitrogen at critical point. Based on the values listed in Table 3, the thermal expansion coefficient (β) values are calculated using RK-EOS, VW-EOS, experimental data (NIST values) and ideal gas equations and these are listed in **Tables 4-7**. With the help of **Tables 4-7**, the accuracy of RK-EOS model is produced, i.e., the β values which are calculated based on the Redlich-Kwong equation lie close to the experimental values when compared to Van der Waals and ideal gas equations. Further, the graphical interpretation and accuracy of the RK-EOS model is described

through Figs. 3 and 4. The thermodynamic variations observed in β curves for various pressures based on experimental values (NIST values) [61, 62], Redlich-Kwong equation [63], Van der Waals equation [64] and perfect-gas equation [65] are demonstrated with the aid of the Figs. 3 and 4. Moreover, to draw the β curve for a perfect gas, we have used the equation $\beta = \frac{1}{T'}$ as provided in the literature [39-42, 65]. Additionally, from these figures it is observed that, in case of liquids at low pressure, β is enhanced with increasing temperature values. However, in the case of gases at low pressure, exactly the opposite trend is noticed. Further, the isotherms at high pressure exhibit liquid-like behavior for small temperature values. However, the isotherms at greater temperature values show gas-like behavior. Additionally, these isotherms attain the peak value at trans-critical temperature and may not be equal to critical temperature. Also, it is clear that, once the temperature and pressure of non-supercritical fluids approach the thermodynamic critical point, then β diverges and the assumption of a constant β produces erroneous results in the supercritical fluid region. Effectively Figs. 3 and 4 indicate that *all isotherms attain the ideal behavior usually at supercritical temperatures*.

Figure 5 is plotted by considering Nu_X (local Nusselt number) against Ra_X (local Rayleigh number) for the present flow configuration in the SCF region. To fit the experimental data, following empirical correlation [66] is used.

$$\frac{Nu_X}{Ra_X^{1/4}} = \frac{4}{3}\left\{\frac{7\,Pr}{5(20+21Pr)}\right\}^{1/4} + \frac{4(272+315Pr)}{35(64+63Pr)}\left\{\frac{d}{l}Ra_X^{1/4}\right\}^{-1} \tag{22}$$

With the help of experimental data [61, 62], the experimental correlation curve is plotted using Eq. (22) in SCF region. Figure 5 clearly demonstrates that the Redlich-Kwong equation of state is the best EOS approach to predict the thermodynamic behavior of couple stress fluid in the SCF region, since, the RK-EOS curve in Fig. 5 lies in the proximity of the experimental curve. This fact once again confirms that, RK-EOS is the best appreciable model to analyze the thermodynamic behavior of different fluids in supercritical region.

5.2. Thermodynamic flow profiles

The time-dependent and time-independent behavior of velocity and temperature fields at various locations (i.e., close to and away from the hot cylindrical wall) in the boundary layer region of couple stress fluid in the supercritical region for semi-infinite vertical cylinder was studied numerically. Steady-state U and θ profiles are presented along the r-direction at $X = 1.0$. Further, the numerical results produced in this article based on Crank-Nicolson finite difference scheme were justified by comparing them with those of Rani et al. [67] and current numerical solutions agree closely with the previous results [67]. This comparison is clearly illustrated through Fig. 6. For different sets of flow parameters such as reduced temperature (T_r^*) and reduced pressure (P_r^*), numerical simulations were performed. Thus, the computer-generated numerical data for couple stress fluid in the supercritical region with respect to T_r^* and P_r^* is presented in terms of graphs in the succeeding sections. Also, for the different set of T_r^* and P_r^*, the nitrogen properties such as μ, C_p, ρ, k and β values in SCF region are documented in **Tables 8 and 9**. Further, the influence of T_r^* and P_r^* on natural convection properties of couple stress fluid in the supercritical region are clearly described in **Figs. 7-13** and **Tables 8-11**.

5.3. Velocity field

The influence of P_r^* and T_r^* on time-dependent and steady-state U profiles is visualized in Figs. 7-9. Figures 7 and 8 are presented in order to understand the flow behavior of couple stress fluid near the cylinder surface (1, 3.01) and far away from the cylinder surface (1, 6.01), respectively. Form these figures it is clearly noticed that, in supercritical fluid region, for all P_r^* and T_r^* values, velocity gradually increases with non-dimensional time (t) from zero value at the cylinder wall and attains the temporal peak value then decays until it reaches the time-independent state asymptotically. Further, it is observed that, when the thermal convection process is about to start, the free convection heat transfer is greatly influenced by the heat

conduction process. Soon after, there occurs a time-stage during which heat transfer is dominated by thermal convection rather than conduction with an associated flow acceleration with progression in time t. Additionally, it is noticed that, when this unsteady non-dimensional time period is about to terminate and just prior to the onset of the time-independent state, distinct velocity overshoots arise. Further, far away from the hot cylinder (i.e. at the other location (1, 6.01)), the behavior of transient velocity is almost similar. Thus, it is noticed from Figs. 7(a) and 7(b) that, velocity field is a function of T_r^* and P_r^*, i.e., velocity field is enhanced for increasing values of P_r^* with fixed T_r^*, whereas velocity field is suppressed for enhancing values of T_r^* when P_r^* is fixed. Also, it is worthy to note that, the time to reach the peak value decays for increasing P_r^* values, whereas it is enhanced with an elevation in values of T_r^* and these changes in non-dimensional time t are illustrated in the **Table 10**. Further, the magnitude of velocity overshoots decreases with increase in P_r^* and T_r^*. This is owing to the reason that the size of the momentum diffusion term magnifies (refer to Eqn. (11)) and this in turn depletes the resistance to the supercritical couple stress fluid flow in the vicinity of the temporal peak of velocity in the flow region. Thus, larger velocity overshoots are observed at lower T_r^* values. Further, the opposite behavior is seen far away from the vertical cylinder, which is clearly apparent from the Figs. 8(a) and 8(b) for different P_r^* and T_r^* values. During the early time intervals, in Figs. 8(a) and 8(b) some interesting patterns emerge. From Fig. 8(a) it is noticed that, *larger velocity overshoots* are observed at smaller P_r^* values and From Fig. 8(b) it is remarked that, *larger velocity overshoots* are noticed at higher T_r^* values in SCF region. Further, from these figures quite interesting behavior is observed in the region $0 \leq t \leq 1.8$ and beyond the location (0.01, 2) the parameters P_r^* and T_r^* has a significant effect on flow behavior.

Figures 9(a) and 9(b) clearly illustrates the effect of P_r^* and T_r^* on computer-generated steady-state velocity flow profiles of couple stress fluid in the supercritical region with respect to non-dimensional radial coordinate R at $X = 1.0$. From these figures it is evident that, on the

cylinder wall, velocity U commences with the null value, attains its maxima and thereafter gradually decreases to zero value along radial axis. Further, it is observed that, in the proximity of the cylinder surface, the magnitude of velocity field along axial coordinate is rapidly enhanced as radial coordinate upsurges from $R_{min}(=1)$. The effect of P_r^* with fixed T_r^* on steady-state velocity is described in Fig. 9(a). It is noticed that velocity field is enhanced in the region $R = 1$ to $R = 4.30$ and suppressed in the remaining portion of the solution domain $R > 4.30$ for amplifying values of P_r^*. However, the changes observed in steady-state velocity profile near the boundaries leads to the occurrence of cross flow behavior at the location (0.3, 4.5). Larger velocity profiles are seen for higher values of P_r^*. Additionally, the time-independent state t decreases for magnifying values of P_r^* in SCF region. Similarly, the influence of T_r^* on time-independent state U profile is illustrated with the aid of Fig. 9(b). From this figure it is clear that, the zone of the solution domain $R = 1$ to $R = 4.30$ features decreasing velocity values whereas velocity field is magnified in the region $R > 4.30$ for increasing values of T_r^*. These variations in the steady-state velocity profile near and away from the cylinder surface results in cross-flow behavior at the location (0.25, 5) in the flow region. Further, the impact of velocity diffusion is enhanced with greater values of T_r^* and which leads to the diminished steady-state velocity in the flow region. Also, it is observed that, smaller velocity profiles are noticed at higher values of T_r^*. The time-independent state t is elevated with greater T_r^* values. Further, from Figs. 9(a) and 9(b) it is noticed that, the predominant effect of T_r^* and P_r^* is noticed in the region $0 \leq R \leq 4.5$. All these variations observed in steady-state velocity flow profile are systematically recorded in the **Table 10**.

5.4. Temperature field

The thermodynamic variations in the computer-generated transient and steady-state temperature flow profiles under the influence of P_r^* and T_r^* are presented in the **Figs. 10 and 11**, respectively. Figures 10(a) and 10(b) are plotted at the location (1, 1.34) to predict the

effects of P_r^* and T_r^* on free convection heat transfer characteristics of couple stress fluid in the supercritical region. Figures 10(a) and 10(b) show that, θ profile enhances with non-dimensional t, attains peak value, then decays, again slightly magnifies and terminates to reach the asymptotic time-independent state. A similar thermodynamic behavior is quite natural for θ profile at the other location also. Further, it is clearly observed from the Figs. 10(a) and 10(b) that, in the beginning time-period, the unsteady temperature profile is particularly observable, since all the curves corresponding to different values of P_r^* and T_r^* coincide with one another and then diverge after some time-period. This is attributable is mainly due to the dominance of thermal conduction heat transfer, at the inception of flow, which greatly influences thermal convection currents in the boundary layer regime. Owing to this reason the effect of P_r^* and T_r^* on thermal profile is insignificant at the beginning when compared to the impact noticed in the region $3 \leq t \leq 7$. Figure 10(a) illustrates that the temperature field is suppressed for the magnifying P_r^* values. Also, time to reach the temporal peak value decays with increasing P_r^*. Further, *larger temperature overshoots* are noticed for smaller values of P_r^* values. However, from Fig. 10(b) it is clear that, θ profile is enhanced for magnifying values of T_r^* in the SCF region. Additionally, the non-dimensional time to attain the temporal peak upsurges as T_r^* increases. All these variations computed in the transient temperature profile are also clearly recorded in **Table 10**.

Figure 11(a) and 11(b) depict the influence of P_r^* and T_r^* on computer-generated steady-state temperature profiles of couple stress fluid in the supercritical region with respect to non-dimensional radial coordinate R at $X = 1.0$. From these figures it clear that, the thermal field begins with $\theta = 1$ and slowly decays to ambient fluid temperature ($\theta = 0$) along the radial coordinate. From Fig. 11(a) it is remarked that, the temperature field decays for magnifying values of P_r^*. Also, the steady-state time suppressed for magnifying P_r^*. Further, from Fig. 11(b), it is clear that, the thermal field is an increasing function of T_r^*. In this case

steady-state time is enhanced for magnifying values of T_r^*. Further, the thickness of the thermal boundary layer decreases for increasing values of T_r^*. This decrement is mainly due to the fact that, the magnified T_r^* values greatly decrease the thermal diffusivity which in turn induces a reduction in thermal boundary layer thickness. From these two figures it clear that, there are considerable variations in Fig. 11(b) when compared to Fig. 11(a). Thus, based on this observation it is apparent that the *supercritical heat transfer characteristics of couple stress fluid are greatly influenced by the temperature changes when compared to pressure changes*.

5.5. Physical quantities of interest

In engineering applications, other quantities of interest are the momentum ($\overline{C_f}$) and heat transport ($\overline{Nu}$) coefficients. The coefficients $\overline{C_f}$ and $\overline{Nu}$ yield important information on wall characteristics of thermal convection flows and feature in aerospace (rocket chamber), nuclear, medical and petroleum systems design. They are also greatly relevant to the analysis of unsteady heat transfer in supercritical fluids in pharmaceutical and engineering applications. Thus, the present problem has larger scale engineering interest in the field of chemical and chromatographic industries etc. It is observed from the literature [68] that, high values of skin-friction coefficient are not appropriate to many of the heat transfer processes since in most industries, the higher temperature gradient values compromise material and structural integrity of the boundaries (biomedical materials processing, rocket cooling channels, heat exchangers etc). However, this problem may be controlled in the other thermodynamic mechanisms namely gas turbines. Thus, $\overline{C_f}$ and $\overline{Nu}$ are very important variables in convection studies. In view of this, the numerical values of $\overline{C_f}$ and $\overline{Nu}$ are documented in Table 11 in the SCF region for various P_r^* and T_r^* values. Further, for the purpose of easier numerical computation, the dimensionless equations for $\overline{C_f}$ and $\overline{Nu}$ are derived as follows.

For the present problem the dimensional wall shear stress at the cylinder surface is given as follows

$$\tau_w = \left(\mu \frac{\partial u}{\partial r}\right)_{r=r_o} \tag{23}$$

By making use of non-dimensional numbers given in Eqn. (9), then Eqn. (23) is suitably modified to the following form:

$$\tau_w = \frac{\mu^2 Gr}{\rho r_o^2}\left(\frac{\partial U}{\partial R}\right)_{R=1} \tag{24}$$

In Eqn. (24), the quantity $\left(\frac{\mu^2 Gr}{\rho r_o^2}\right)$ is treated as *characteristic shear stress*. Thus, the equation for *local momentum transport coefficient* can be written as:

$$C_f = \left(\frac{\partial U}{\partial R}\right)_{R=1} \tag{25}$$

At the end, average momentum transport coefficient is produced by integrating Eqn. (25) with respect to X and by considering $X = 0$ to $X = 1$. Thus, the final expression for *average wall shear stress* is as follows:

$$\overline{C_f} = \int_0^1 \left(\frac{\partial U}{\partial R}\right)_{R=1} dX \tag{26}$$

Similarly, the equation for Nusselt number (dimensionless wall heat transfer rate which expresses the relative influence of thermal convection to thermal conduction at the boundary) is derived as follows. In the present case the expression for *local Nusselt number* is taken as follows:

$$Nu_x = \frac{\dot{q}_w r_o}{k(T'_w - T'_\infty)} \tag{27}$$

Here $\dot{q}_w$ denotes the heat transfer flux which is given by

$$\dot{q}_w = -k\left(\frac{\partial T'}{\partial r}\right)_{r=r_o} \tag{28}$$

Invoking the non-dimensional numbers given in Eqn. (9), then Eqn. (28) is suitably transformed into the following form:

$$Nu_X = -\left(\frac{\partial \theta}{\partial R}\right)_{R=1} \tag{29}$$

Thus, the final equation for *average heat transfer rate* is obtained by integrating Eqn. (29) with respect to X by considering $X = 0$ to $X = 1$, yielding the following equation:

$$\overline{Nu} = -\int_0^1 \left(\frac{\partial \theta}{\partial R}\right)_{R=1} dX \tag{30}$$

Thus, Eqns. (26) and (30) are effectively used to calculate the momentum and heat transport coefficients, respectively. Also, a *five-approximation* formula is used to calculate the derivatives $\frac{\partial U}{\partial R}$ and $\frac{\partial \theta}{\partial R}$. Finally, the Newton-Cotes closed integration formula is utilized to solve the resulting integrals.

The influence of P_r^* and T_r^* on $\overline{C_f}$ is illustrated in **Figs. 12(a) and 12(b).** Figures 12(a) and 12(b) shows that, at first $\overline{C_f}$ enhances with non-dimensional time t, attains its maximum values, then decreases and eventually reaches the steady-state at the end of the time-period. Figure 12(a) illustrates that, $\overline{C_f}$ increases as P_r^* magnifies (see also Table 11). This is due to the velocity field being enhanced in the proximity of the hot cylinder surface, as already discussed in the Figs. 7(a) and 9(a). Also, it is noticed from Fig. 12(a) that, the non-dimensional time t required to attain maximum value of $\overline{C_f}$ decrease as P_r^* increases. Further, the magnitude of $\overline{C_f}$ overshoots increase with upsurge in P_r^*. Similarly, Fig. 12(b) indicates that, $\overline{C_f}$ is suppressed for magnifying T_r^* values (refer to Table 11). Since, velocity field decreases in the proximity of cylinder surface as already described in Figs. 7(b) and 9(b). Further, the magnitude of $\overline{C_f}$ overshoots decreases with increase in T_r^*. Also, the time to attain the maximum value upsurges with increment in T_r^*. Further, from these figures it is evident that the influence of control parameters on heat transfer characteristics couple stress fluid are prominent beyond the region $0.5 \leq t$, when compared to $t \leq 0.5$. This fact is due the dominance of thermal convection process in SCF region. All these changes observed in the $\overline{C_f}$ profiles for different values of P_r^* and T_r^* are also provided in **Table 11**.

Similarly, the effect of P_r^* and T_r^* on $\overline{Nu}$ over the non-dimensional time t in supercritical region is illustrated through **Figs. 13(a) and 13(b).** From these two figures it is evident that, for all the values of P_r^* and T_r^*, the $\overline{Nu}$ curves overlap with one another during the early time period (i.e. $t = 0$) and they diverge from one another after some time t, again since thermal conduction dominates the convective heat transfer in the beginning time. Thus, free convection heat transfer is mainly due to the conduction process at the starting time. From Fig. 13(a) it is noticed that, $\overline{Nu}$ is elevated with increase in P_r^* values (refer to Table 11). Since, an upsurge in P_r^* increases the spatial decay of the temperature field in the proximity of hot cylinder surface together with the magnified velocity field close to the hot wall, this manifests in an upsurge in the average heat transfer rate. However, the effect of P_r^* and T_r^* on $\overline{Nu}$ profile is dominant beyond the region $2.0 \leq t$ when compared to the region $t \leq 2$. It is noticed that, the magnitude of $\overline{Nu}$ overshoots increase with increase in P_r^* values. Also, the non-dimensional time t required for $\overline{Nu}$ to reach its maximum value decreases with elevation in P_r^* values. Similarly, from Fig. 13(b) it is clear that, the $\overline{Nu}$ profile is suppressed with increasing T_r^* values (refer again to Table 11). Since, temperature field increases for increasing values of T_r^* (refer Fig. 11(b)), this produces the negatively increasing values in Nusselt number profile (refer to Eqn. 30). It is observed that, the magnitudes of the $\overline{Nu}$ overshoots eventually decrease with upsurge in T_r^* values. Also, the non-dimensional time t required for $\overline{Nu}$ to reach its peak value increases with upsurge in T_r^*. Again, all these variations in $\overline{Nu}$ profile magnitudes for various values of P_r^* and T_r^* are systematically listed in the Table 11.

Further, the influence of P_r^* and T_r^* on local Nusselt number (Nu_X) profile with respect to local Rayleigh number (Ra_X) in the supercritical region for couple stress fluid are illustrated in the Figs. 14(a) and 14(b). Also, during the beginning time interval all the Nu_X curves are coincident and subsequently deviate from one another after some time. From Fig. 14(a) it is apparent that the Nu_X profiles are reduced with increasing values of P_r^* in the SCF region.

Similarly, from Fig. 14(b) it is clear that, the Nu_X profile is enhanced for increasing values of T_r^*. From these two figures it is clear that, Fig. 14(b) exhibits greater variation as compared to Fig. 14(a), which signifies that, the *effect of pressure is markedly less than temperature*. However, the small change in thermal field produces the considerable vicissitudes in the Nu_X profile, which is illustrated in the Figs. 14(a) and 14(b). Thus, it is clear from the above numerical discussion that, effect temperature on SCF is considerably greater when compared to pressure.

5.6. Heat flow visualization in supercritical fluid region

In order to describe the heat flow in supercritical region we have used Bejan's heat line visualization concept in this paper. For this purpose, we have utilized $U = \frac{1}{R}\frac{\partial \psi}{\partial R}$ and $V = -\frac{1}{R}\frac{\partial \psi}{\partial X}$. Thus, the heat function (H^*) is well-defined with the following coupled equations:

$$\frac{\partial \mathrm{H}^*}{\partial x} = \rho v r c_p (T' - T'_\infty) - kr\frac{\partial T'}{\partial r} \tag{31}$$

$$-\frac{1}{r}\frac{\partial \mathrm{H}^*}{\partial r} = \rho u c_p (T' - T'_\infty) \tag{32}$$

The dimensional H^* identically obeys the temperature Eqn. (3). For the non-dimensional case, the dimensionless heat function (H) is defined as $\mathrm{H} = \frac{H^*}{k(T'-T'_\infty)r_o Gr^{11/12}}$. From the definition of H it is clear that, the maximum values of H and $\overline{Nu}$ are same on the hot wall of the cylinder [69, 70]. Using definition of H, Eqns. (31) and (32) are non-dimensionalized as follows:

$$\frac{\partial \mathrm{H}}{\partial X} = Pr(RV\theta) - R\frac{\partial \theta}{\partial R} \tag{33}$$

$$-\frac{\partial \mathrm{H}}{\partial R} = Pr(RU\theta) - R\frac{\partial \theta}{\partial R} \tag{34}$$

From Eqns. (33) and (34) it is clear that, H identically satisfies the dimensionless time-independent state thermal Eqn. (12). The literature [55, 69, 70] provides a clear picture of these derivations and appropriate boundary conditions.

The present research article suitably uses a stream function (ψ) to portray the thermodynamic behavior of couple stress fluid in the supercritical region. Further, second order finite difference computation is efficiently utilized to calculate the stream function (ψ) and heat function (H). However, for the different set of P_r^* and T_r^* values, the time-independent state characteristics of streamlines, isotherms and heat lines are illustrated in Figs. 15-17. The thermodynamic variations in the streamlines profile is described through **Figs. 15 (a) and 15(b)**. The variation of ψ with respect to P_r^* in the SCF region is illustrated in Fig. 15(a). It is noticed from Fig. 15(a) that, streamlines move away from the hot cylindrical wall for magnifying values of P_r^*. Also, the changes observed in ψ profile with respect to T_r^* in the SCF region are demonstrated in Fig. 15(b). It is clear from Fig. 15(b) that, streamlines converge towards the hot cylinder surface with increasing values of T_r^*. Further, it is observed from the literature that, heat lines are more appropriate tools for heat flow visualization in two-dimensional solution domains when compared to isotherms and streamlines. Similarly, Figs. 16(a) and 16(b) describe the effect of P_r^* and T_r^* on heat line profiles (H) in the SCF region respectively. From Fig. 16(a) it is observed that, for increasing values of P_r^*, the heat lines profile migrates away from the cylinder surface. Also, with an elevation in values of T_r^* in the SCF region, heat line profiles are intensified in the vicinity of cylinder surface. This implies that the effect of temperature on heat line distributions is substantially greater when compared to pressure in the supercritical fluid region. The influence of P_r^* and T_r^* on isotherms is detailed in Figs. 17(a) and 17(b), respectively. Figure 17(a) indicates that the isotherm profiles occur closer to the hot wall for increasing values of P_r^*. Similarly, isotherm profile depart increasingly from the hot surface when T_r^* increases. Further, it is apparent that a greater concentration of heat lines occurs in the vicinity of the hot cylinder surface in comparison with streamlines. This fact is attributable to the prescription of a no-slip condition on the hot cylindrical wall; the heat flux is closer to the hot cylinder surface when compared to the velocity values. With the above

heat flow visualization trends, it may be deduced that *temperature is the dominant factor when compared to pressure in the supercritical region for couple stress fluids*.

6. CONCLUSIONS

Utilizing the equation of state (EOS) approach, a two-dimensional mathematical model has been derived to simulate the *free convection boundary layer flow external to a vertical cylinder for a couple stress fluid in the supercritical flow (SCF) region*. The popular RK-EOS and VW-EOS approaches have been deployed for thermodynamic analysis. These thermodynamic state models have been used to derive a suitable equation for the coefficient of thermal expansion (β) in supercritical region. From graphical and tabulated numerical data, it is observed that, β values calculated using the RK-EOS approach lie in the proximity of experimental values when compared to perfect gas and VW-EOS approaches. Thus, the present thermodynamic analysis demonstrates that to solve time-dependent free convection flow problems in the SCF region, the RK-EOS is the most robust model. The current work has further added the Bejan's heat flow concept to further analyze heat transfer characteristics in free convection couple stress flow in the supercritical flow (SCF) region. Nitrogen gas has been considered. The non-dimensional conservation boundary layer equations governing the flow of supercritical couple stress fluid over a semi-infinite cylinder have been solved computationally with Crank-Nicolson finite difference method. Grid independence and time independence tests have also been included. Validations with published experimental and theoretical results from the literature have also been provided confirming the accuracy of the Crank-Nicolson algorithm. Simulations are executed with respect to reduced pressure and reduce temperature. The present computations have shown that.

- Supercritical heat transfer characteristics of couple stress fluid vary significantly with temperature field when compared to pressure changes.

- The β values calculated based on the RK-EOS methodology achieve closer correlation with experimental values when compared to ideal gas and VW-EOS thermodynamic approaches.
- Average skin-friction coefficient is eventually magnified in the SCF region with greater values of reduced pressure (P_r^*), whereas the converse trend is observed for increasing values of reduced temperature (T_r^*).
- Average heat transfer rate exhibits an increasing trend with greater P_r^* values, whereas it is markedly suppressed with larger values of T_r^* in SCF region.
- Streamline profiles move away from the hot wall when P_r^* increases in the SCF region.
- Heat line profiles converge closer to the hot cylinder wall for greater values of T_r^*.
- Velocity field is an increasing function of reduced pressure in the supercritical region for couple stress fluid.
- Magnifying values of reduced temperature decrease the velocity field (i.e. induce flow deceleration) in the supercritical fluid region.
- Thermal field decays with greater P_r^* whereas the thermal profile is observed to be an increasing function of T_r^*.
- The time required to reach the steady-state decreases with an increase in P_r^* and it is elevated with larger values of reduced temperature, T_r^*.
- The Crank-Nicolson numerical method achieves exceptional convergence and accuracy in nonlinear thermofluid dynamics simulations of non-Newtonian micro-structural fluids and is presently being employed (in addition to other numerical methods such as finite volume methods) to consider other supercritical heat transfer problems of relevance in aerospace rocket cooling [71] and bio-nano-material synthesis [72].

ACKNOWLEDGEMENTS:

The first author Hussain Basha wishes to thank Maulana Azad National Fellowship program, University Grants Commission, Government of India, Ministry of Minority Affairs, MANF (F1-17.1/2017-18/MANF-2017-18-KAR-81943) for the grant of research fellowship and to Central University of Karnataka for providing the research facilities. The authors are thankful to reviewers for their valuable suggestions and comments which have improved the quality of the manuscript.

REFERENCES

1. V. K. Stokes, Couple stresses in fluids, Physics Fluids 9 (1966) 1710-1715.
2. V. K. Stokes, Theories of Fluids with Microstructure, Springer-Verlag, New York, Tokyo (1984).
3. G. Ramanaiah, Squeeze films between finite plates lubricated by fluids with couple-stresses, Wear 54 (1979) 315-320.
4. P. Sinha and C. Singh, Couple stress in the lubrication of rolling contact bearings considering cavitation, Wear 67 (1981) 85-91.
5. C. Singh, Lubrication theory for couple stress fluids and its application to short bearings, Wear 80 (1982) 281-290.
6. R. S. Gupta and R. L. Sharma, Analysis of couple stresses lubricant in hydrostatic thrust bearings, Wear 48 (1988) 257-69.
7. U. M. Mokhiamer, W. A. Crosby and H. A. El-Gamel, A study of journal bearing lubricated by fluids with couple stresses considering the elasticity of the liner, Wear 224 (1999)194-201.
8. S. Islam and C. Y. Zhou, Exact solutions for two dimensional flows of couple stress fluids, Z. Angew. Math. Phys. 58 (2007) 1035-1048.

9. K. C. Valanis and C. T. Sun, Poiseuille flow of a fluid with couple stress with applications to blood flow, Biorheology 6 (1969) 85-97.
10. L. M. Srivastava, Peristaltic transport of a couple stress fluid, Rheologica Acta 25(1986) 638-641.
11. H. L. Agrawal and B. Anwaruddin, Peristaltic flow of blood in a branch, Ranchi University mathematical journal 15(1984)111-15.
12. L. M. Srivastava, Flow of couple stress fluid through stenotic blood vessels, Journal of Biomechanics 18(7) (1985) 479-485.
13. S. Maiti and J. C. Misra, Peristaltic transport of a couple stress fluid: Some applications to hemodynamics, Journal of Mechanics in Medicine and Biology 2(3) (2012) 1250048-21.
14. J. V. Ramana Murthy, J. Srinivas and O. Anwar Bég, Entropy generation analysis of radiative heat transfer effects on channel flow of two immiscible couple stress fluids, J. Brazilian Soc. Mech Sci. Eng, 39, 2191–2202 (2017).
15. N. Ali, M. Sajid, Z. Abbas and O. Anwar Bég, Swimming of micro-organism in a fluid with couple stresses - a rheological model of embryological hydrodynamic propulsion, J. Mechanics in Medicine and Biology 17 (3) 1750054.1- 1750054.23 (2017).
16. J. C. Misra D. Tripathi, A. Yadav and O. Anwar Bég, Electro-osmotic flow of couple stress fluids in a micro-channel propagated by peristalsis, European Physical Journal Plus (Italy) 132: 173-185. (2017).
17. M. Shamshuddin, Siva Reddy Sheri and O Anwar Bég, Oscillatory dissipative conjugate heat and mass transfer in chemically reacting micropolar flow with wall couple stress: A finite element numerical study, Proc IMechE Part E: J Process Mechanical Engineering (2017). DOI: 10.1177/0954408917743372 (17 pages).

18. D. Tripathi and O. Anwar Bég, Transient magneto-peristaltic flow of couple stress biofluids: a magneto-hydro-dynamical study on digestive transport phenomena, Mathematical Biosciences, 246 (1):72-83 (2013).

19. K. A. Larson and M. L. King, Evaluation of supercritical fluid extraction in the pharmaceutical industry, Biotechnology Progress 2(2) (1986) 73-82.
20. C. A. Eckert, B. L. Knutson and P. G. Debenedetti, Supercritical fluids as solvents for chemical and materials processing, Nature 383 (1996) 313-318.
21. B. Subramaniam, R. A. Rajewski, and K. Snavely, Pharmaceutical processing with supercritical carbon dioxide, Journal of Pharmaceutical Sciences 86(8) (1997) 885-890.
22. M. Perrut, Supercritical fluid applications: Industrial developments and economic issues, Industrial & Engineering Chemistry Research 39 (2000) 4531-4535.
23. J. Jung and M. Perrut, Particle design using supercritical fluids: Literature and patent survey, Journal of Supercritical Fluids 20 (2001) 179-219.
24. N. Blagden, M. de Matas, P. T. Gavan and P. York, Crystal engineering of active pharmaceutical ingredients to improve solubility and dissolution rates, Advanced Drug Delivery Reviews 59 (2007) 617-630.
25. Z. Knez, E. Markocic, M. Leitgeb, M. Primozic, M. Knez Hrncic and M. Skerget, Industrial applications of supercritical fluids: A review, Energy 77 (2014) 235-243.
26. T. Adschiri and A. Yoko, Supercritical fluids for nanotechnology, The Journal of Supercritical Fluids 134 (2018) 167-175.
27. E. Kiran, P. G. Debenedetti and C. J. Peters, Supercritical fluids: Fundamental and applications, NATO science series, Springer (2000).
28. Y. Arai, T. Sako and Y. Takebayashi, Supercritical fluids, Springer-Verlag Berlin Heidelberg, first edition (2002).
29. A. Bejan, Convection Heat Transfer, John Wiley & Sons, Inc. (2013).

30. E. M. Sparrow and J. L. Gregg, Laminar free convection heat transfer from the outer surface of a vertical circular cylinder, Journal of Heat Transfer 78(8) (1956) 1823-1829.
31. H. R. Lee, T. S. Chen and B. F. Armaly, Natural convection along slender vertical cylinders with variable surface temperature, Journal of Heat Transfer 110(1) (1988)103-108.
32. M. A. McHugh and V. J. Krukonis, Supercritical fluid extraction, principles and practice, Second ed., Butterworth-Heinemann, Boston (1994).
33. R. J. Neumann and E. W. P. Hahne, Free convective heat transfer to supercritical carbon dioxide, International Journal of Heat Mass Transfer 23(12) (1980) 1643-1652.
34. K. Nishikawa, T. Ito and H. Yamashita, Free-convective heat transfer to supercritical fluid, Journal of Heat Transfer 95(2) (1973) 187-191.
35. E. W. P. Hahne, Natural convection heat transfer through an enclosed horizontal layer of supercritical carbon dioxide, International Journal of Heat Mass Transfer 1(3) (1968) 190-196.
36. E. A. Muller and L. A. Estevez, Mixing expansivities and Grashof number in supercritical fluids using cubic equations-of-state, The Journal of Supercritical Fluids 3(1990) 136-142.
37. K. Nishikawa and T. Ito, An analysis of free-convective heat transfer from an isothermal vertical plate to supercritical fluids, International Journal of Heat and Mass Transfer 12 (1969) 1449-1463.
38. A. Rolando, Natural convection heat transfer in supercritical fluids, M.Sc. Thesis, Mechanical Engineering, University of Puerto Rico (2004).
39. A. R. Teymourtash, D. R. Khonakdar and M. R. Raveshi, Natural convection on a vertical plate with variable heat flux in supercritical fluids, The Journal Supercritical Fluids, 74 (2013) 115-127.

40. D. R. Khonakdar and M. R. Raveshi, Mixed convection on a vertical plate in supercritical fluids by selecting the best equation of state, The Journal Supercritical Fluids, 107 (2016) 549-559.
41. G. J. Reddy, H. Basha and N. S. V. Narayanan, Transient natural convection heat transfer to CO_2 in the supercritical region, Journal of Heat Transfer, 140 (2018) 092502-10.
42. G. J. Reddy, H. Basha and N. S. Venkata Narayanan, A numerical investigation of transient natural convective heat transfer to isobutane in the supercritical region, Journal of Molecular Liquids 250 (2018) 131-149.
43. Urbano, A., Pizzarelli, M., and Nasuti, F., Numerical analysis of transcritical fluids heating in liquid rocket engine cooling channels, Aerotecnica Missili E Spazio, Vol. 88, (2009) 20– 30.
44. V. Goodship and E. O. Ogur, Polymer processing with supercritical fluids, Rapra Review Reports, USA (2004).
45. D. B. Kimmel, Mechanism of action, pharmacokinetic and pharmacodynamic profile, and clinical applications of nitrogen-containing bisphosphonates, Journal of Dental Research 86(11) (2007)1022-1033.
46. M. Talha, C. K. Behera and O. P. Sinha, A review on nickel-free nitrogen containing austenitic stainless steels for biomedical applications, Materials Science and Engineering C 33 (2013) 3563-3575.
47. Y. Gorbaty and G. V. Bondarenko, Transition of liquid water to the supercritical state, Journal of Molecular Liquids 239 (2016) 5-9.
48. M. Chopra and N. Choudhury, Structural and dynamical aspects of uranyl ions in supercritical water: a molecular dynamics simulation study, Journal of Molecular Liquids 224 (2016) 599-606.

49. A. B. Solovieva, A. V. Cherkasova, N. N. Glagolev, A. S. Kopylov, P. S. Timashev, S. I. Tsypina and V. N. Bagratashvili, Stable “coloured” states of spirooxazine photochrom molecules immobilized in polymer matrixes by supercritical carbon dioxide, Journal of Molecular Liquids 239 (2017) 74-82.
50. M. Zhang, M. Dou, M. Wang and Y. Yu, Study on the solubility parameter of supercritical carbon dioxide system by molecular dynamics simulation, Journal of Molecular Liquids 248 (2017) 322-329.
51. S. Artemenko, P. Krijgsman and V. Mazur, The Widom line for supercritical fluids, Journal of Molecular Liquids 238 (2017) 122-128.
52. H. Bagheri, G. A. Mansoori and H. Hashemipour, A novel approach to predict drugs solubility in supercritical solvents for RESS process using various cubic EoS-mixing rule, Journal of Molecular Liquids 261 (2018) 174-188.
53. S. Mohammed and G. A. Mansoori, Molecular insights on the interfacial and transport properties of supercritical CO_2/brine/crude oil ternary system, Journal of Molecular Liquids 263 (2018) 268-273.
54. V. K. Yadav, Vibrational spectral diffusion in supercritical deuterated ammonia from first principles simulations: Roles of hydrogen bonds, free ND modes and inertial rotation of ammonia molecules, Journal of Molecular Liquids 269 (2018) 896-904.
55. H. P. Rani, G. J. Reddy, C. N. Kim and Y. Rameshwar, Transient couple stress fluid past a vertical cylinder with Bejan’s heat and mass flow visualization for steady-state, Journal of Heat Transfer 137 (2015) 032501-12.
56. B. Carnahan, H. A. Luther and J. O. Wilkes, Applied Numerical Methods, John Wiley and Sons, New York (1969).
57. D. U. Von Rosenberg, Methods for the Numerical Solution of Partial Differential Equations, American Elsevier Publishing Company, New York (1969).

58. P. Ganesan and H. P. Rani, Transient natural convection along vertical cylinder with heat and mass transfer, Heat and Mass Transfer 33(1998) 449-455.
59. H. P. Rani, G. J. Reddy and C. N. Kim, Transient analysis of diffusive chemical reactive species for couple stress fluid flow over vertical cylinder, Applied Mathematics and Mechanics (English Edition) 34(8) (2013) 985-1000.
60. G. J. Reddy, H. Basha and N. S. V. Narayanan, Finite difference analysis of unsteady natural convection properties of carbon dioxide in the supercritical region using the Redlich-Kwong equation of state, Journal of Physics and Chemistry of Solids 122 (2018) 284-301.
61. NIST (National Institute of Standards and Technology) Chemistry Web Book (http://webbook.nist.gov/chemistry/fluid/).
62. R. Span, E. W. Lemmon, R. T. Jacobsen, W. Wagner and A. Yokozeki, A reference equation of state for the thermodynamic properties of nitrogen for temperatures from 63.151 to 1000 K and pressures to 2200 MPa, Journal of Physical and Chemical Reference Data, 29 (6) (2000) 1361-1433.
63. G. Soave, 20 years of Redlich-Kwong equation of state, Fluid phase equilibria 82 (1993) 345-359.
64. S. J. Blundell and K. M. Blundell, Concepts in Thermal Physics, Oxford University Press (2006).
65. B. E. Poling, J. M. Prausnitz and J. P. O'Connell, The properties of gases and liquids, fifth edition, McGraw-Hill, New York (2001).
66. A. J. Ede, Advances in Free Convection, National Engineering Laboratory, East Kilbride, Scotland, UK (1967).

67. H. P. Rani, G. J. Reddy and C. N. Kim, Numerical analysis of couple stress fluid past an infinite vertical cylinder, Engineering Applications of Computational Fluid Mechanics, 5(2) (2011) 159-169.

68. H. P. Rani and G. J. Reddy, Conjugate transient free convective heat transfer from a vertical slender hollow cylinder with heat generation effect, Applied Mathematics, 1(2) (2011) 90-98.

69. S. Kimura and A. Bejan, The heatline visualization of convective heat transfer, ASME Journal of Heat Transfer 105(4) (1983) 916-919.

70. S. K. Aggarwal and A. Manhapra, Use of heat lines for unsteady buoyancy-driven flow in a cylindrical enclosure, ASME Journal of Heat Transfer, 111(2) (1989) 576-578.

71. O. Anwar Bég, A. Zubair, S. Kuharat and M. Babaie, CFD simulation of turbulent convective heat transfer in rectangular mini-channels for rocket (super-critical) cooling applications, ICHTFM 2018: 20th International Conference on Heat Transfer and Fluid Mechanics, Istanbul, Turkey, August 16-17 (2018).

72. N. Shukla, Puneet Rana, O. Anwar Bég, A. Kadir and Bani Singh, Unsteady electromagnetic radiative nanofluid stagnation-point flow from a stretching sheet with chemically reactive nanoparticles, Stefan blowing effect and entropy generation, Proc. IMechE: Part N-Journal of Nanomaterials, Nanoengineering and Nanosystems (2018). DOI:10.1177/2397791418782030(14pages).

Table 1. Grid independence test for selecting mesh size for fixed $P_r^* = 1.82$ and $T_r^* = 2.61$.

Grid size	Maximum velocity (U) at $X = 1.0$	Average skin-friction coefficient ($\overline{C_f}$)	Average heat transfer rate ($\overline{Nu}$)
25X125	0.42577023	0.21613580	0.94776640
50X250	0.43699978	0.14660650	0.92744670
100X500	0.44249711	0.08677714	0.91997920
200X1000	0.44249634	0.08677698	0.91997740

Table 2. Grid independence test for choosing time step size for fixed $P_r^* = 1.82$ and $T_r^* = 2.61$.

Time step size Δt	Maximum velocity (U) at $X = 1.0$	Average skin-friction coefficient ($\overline{C_f}$)	Average heat transfer rate ($\overline{Nu}$)
0.8	0.44297709	0.08676671	0.92013480
0.5	0.44268989	0.08676267	0.91990080
0.04	0.44248248	0.08676877	0.91994080
0.03	0.44257162	0.08677130	0.91996920
0.02	0.44251455	0.08677378	0.91998350
0.01	0.44251211	0.08677314	0.91998120

Table 3. Critical values of nitrogen [61, 62] for calculating flow parameters.

Chemical compound	P_c (MPa)	T_c (K)	M (kg/mol)	D_c (kg/m^3)
Nitrogen	3.3958	126.192	0.0140067	313.300

Table 4. Thermal expansion coefficient (β) values based on RK-EOS [63] for different values of reduced pressure (P_r^*) and reduced temperature (T_r^*) in SCF region.

P (MPa)	P_r^*	T' (K)	T_r^*	A	B	Z	β (1/K)
4.0	1.17	260	2.06	0.082638	0.049521	0.972803	0.00441821
4.2	1.23	270	2.13	0.078957	0.050071	0.977145	0.00421049
4.4	1.29	280	2.21	0.075528	0.050582	0.981151	0.00402157
4.6	1.35	290	2.29	0.072329	0.051058	0.984856	0.00384903
4.8	1.41	300	2.37	0.069341	0.051502	0.988290	0.00369083

Table 5. Thermal expansion coefficient (β) values based on VW-EOS [64] for different values of reduced pressure (P_r^*) and reduced temperature (T_r^*) in SCF region.

P (MPa)	P_r^*	T' (K)	T_r^*	A	B	Z	β (1/K)
4.0	1.17	260	2.06	0.117062	0.071463	0.958431	0.00450103
4.2	1.23	270	2.13	0.113979	0.072257	0.962754	0.00429596
4.4	1.29	280	2.21	0.111030	0.072995	0.966825	0.00410827
4.6	1.35	290	2.29	0.108209	0.073681	0.970663	0.00393590
4.8	1.41	300	2.37	0.105512	0.074322	0.974286	0.00377710

Table 6. Thermal expansion coefficient (β) values based on experimental data [61, 62] for different values of reduced pressure (P_r^*) and reduced temperature (T_r^*) in SCF region.

P (MPa)	P_r^*	T' (K)	T_r^*	β (1/K)
4.0	1.17	260	2.06	0. 00429985
4.2	1.23	270	2.13	0.00410393
4.4	1.29	280	2.21	0.00392441
4.6	1.35	290	2.29	0.00376052
4.8	1.41	300	2.37	0.00360954

Table 7. Thermal expansion coefficient (β) values based on ideal gas assumption [65] for different values of reduced pressure (P_r^*) and reduced temperature (T_r^*) in SCF region.

P (MPa)	P_r^*	T' (K)	T_r^*	β (1/K)
4.0	1.17	260	2.06	0.00384615
4.2	1.23	270	2.13	0.00370370
4.4	1.29	280	2.21	0.00357142
4.6	1.35	290	2.29	0.00344827
4.8	1.41	300	2.37	0.00333333

Table 8. Thermal expansion coefficient values based on RK-EOS for fixed $P_r^* = 1.82$ in supercritical region.

P (MPa)	P_r^*	T' (K)	T_r^*	C_p (J/mol*K)	μ (10^{-6} Pa*s)	k (W/m*K)	ρ (Kg/m^3)	β (1/K)
6.2	1.82	260	206	33.248	17.379	0.026668	82.544	0.00468066
6.2	1. 82	270	2.13	32.827	17.789	0.027196	78.874	0.00440780
6.2	1. 82	280	2.21	32.472	18.200	0.027729	75.561	0.00416948
6.2	1. 82	290	2.29	32.170	18.612	0.028266	72.551	0.00395920
6.2	1. 82	300	2.37	31.911	19.023	0.028807	69.800	0.00377204

Table 9. Thermal expansion coefficient values based on RK-EOS for fixed $T_r^* = 1.86$ in supercritical region.

P (MPa)	P_r^*	T' (K)	T_r^*	C_p (J/mol*K)	μ (10^{-6} Pa*s)	k (W/m*K)	ρ (kg/m^3)	β (1/K)
4.0	1.17	235	1.86	32.646	15.686	0.023643	59.590	0.00514781
4.2	1.23	235	1.86	32.833	15.743	0.023799	62.670	0.00518997
4.4	1.29	235	1.86	33.021	15.801	0.023958	65.756	0.00523166
4.6	1.35	235	1.86	33.209	15.860	0.024118	68.850	0.00527284
4.8	1.41	235	1.86	33.398	15.920	0.024281	71.950	0.00531347

Table 10. Time to reach temporal maxima of flow variables, steady-state and maximum velocity at $X = 1.0$ with various values of P_r^* and T_r^* for supercritical nitrogen.

P_r^*	T_r^*	Temporal maximum (t) of U	Temporal maximum (t) of θ	Steady-state time	Maximum velocity (U) at $X = 1.0$
1.17	1.86	3.58	3.66	6.65	0.63156090
1.23	1.86	3.41	3.51	6.35	0.65842779
1.29	1.86	3.30	3.42	6.06	0.68574792
1.35	1.86	3.18	3.28	5.80	0.71295660
1.41	1.86	3.06	3.12	5.56	0.74061257
1.82	2.06	3.12	3.15	5.61	0.73560162
1.82	2.13	3.38	3.43	6.16	0.67701403
1.82	2.21	3.61	3.70	6.73	0.62560574
1.82	2.29	3.90	3.95	7.27	0.58023980
1.82	2.37	4.17	4.24	7.79	0.54013729

Table 11. Average skin-friction coefficient ($\overline{C_f}$) and Nusselt number ($\overline{Nu}$) for different values of P_r^* and T_r^* for nitrogen in supercritical region.

P_r^*	T_r^*	$\overline{C_f}$	$\overline{Nu}$
1.17	1.86	0.15010840	1.02808400
1.23	1.86	0.16020970	1.04239200
1.29	1.86	0.17049490	1.05550200
1.35	1.86	0.18101650	1.06848700
1.41	1.86	0.19180710	1.08067400
1.82	2.06	0.18904970	1.07470600
1.82	2.13	0.16639060	1.04713000
1.82	2.21	0.14737500	1.02168400
1.82	2.29	0.13128370	0.99811290
1.82	2.37	0.11759280	0.97624300

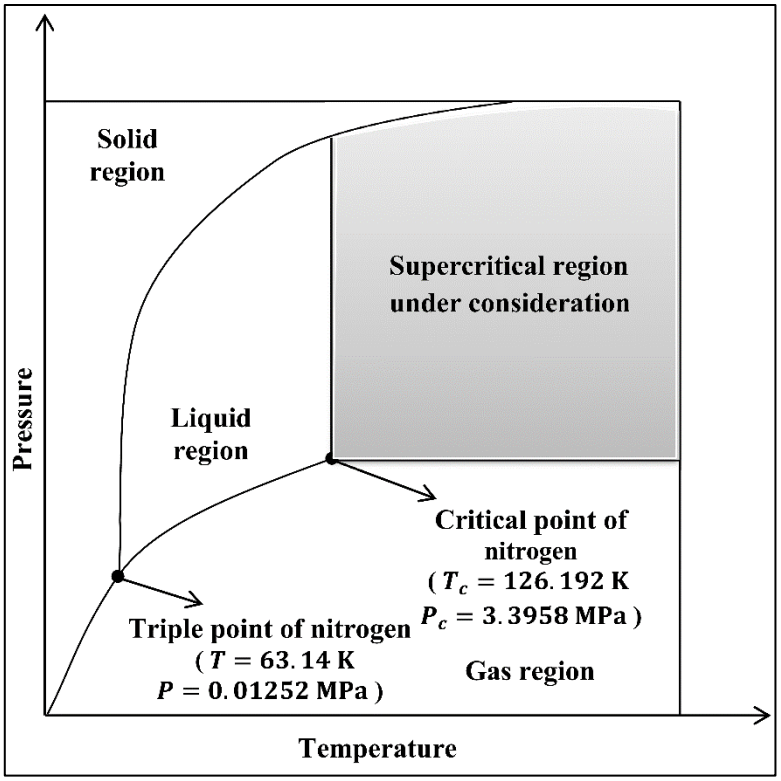

Fig. 1. Idealized phase diagram with SCF region under consideration.

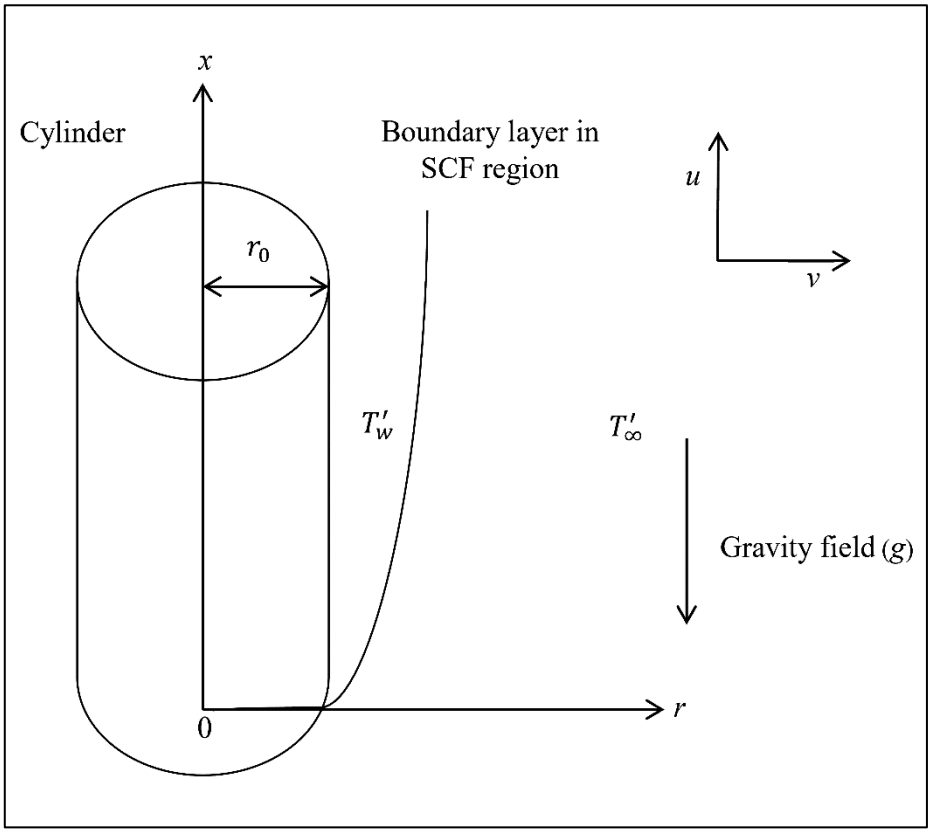

Fig. 2. Flow configuration of the investigated problem.

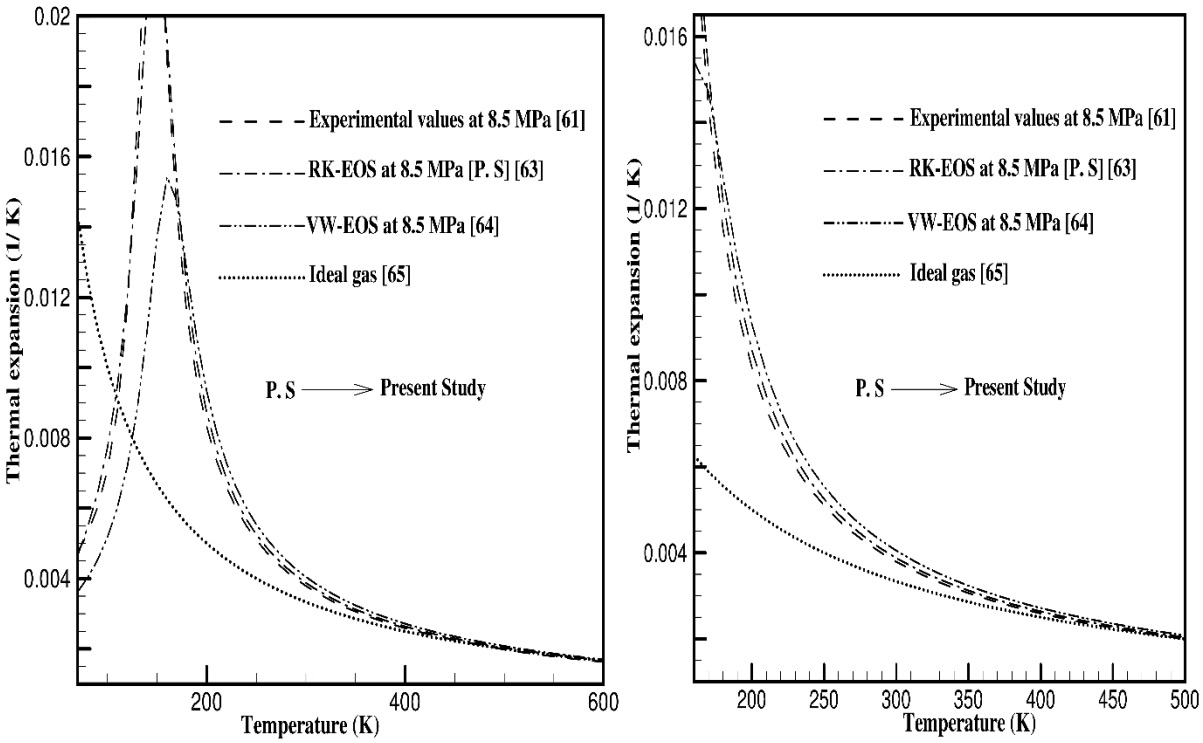

(a) (b)

Fig. 3. (a) Comparison between β of nitrogen based on experimental data [61], RK-EOS [63], VW-EOS [64] with ideal gas [65] at 8.5 MPa (b) close up.

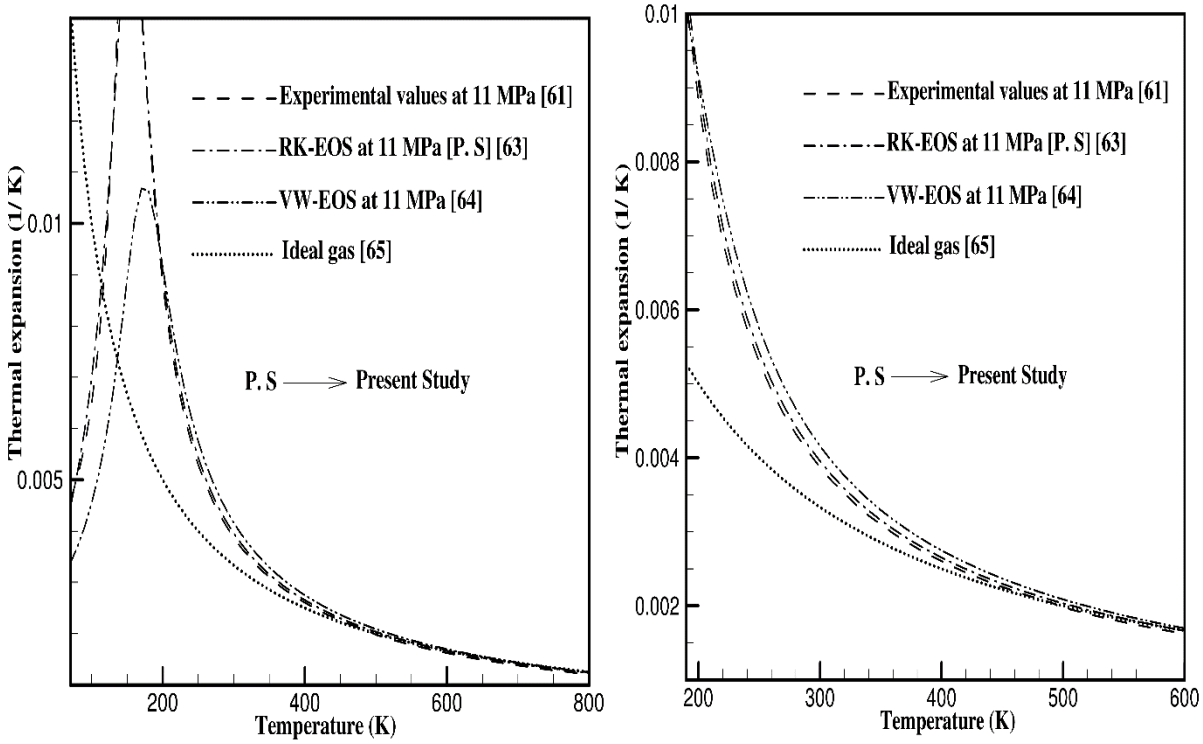

(a) (b)

Fig. 4. (a) Comparison between β of nitrogen based on experimental data [61], RK-EOS [63], VW-EOS [64] with ideal gas [65] at 11 MPa (b) close up.

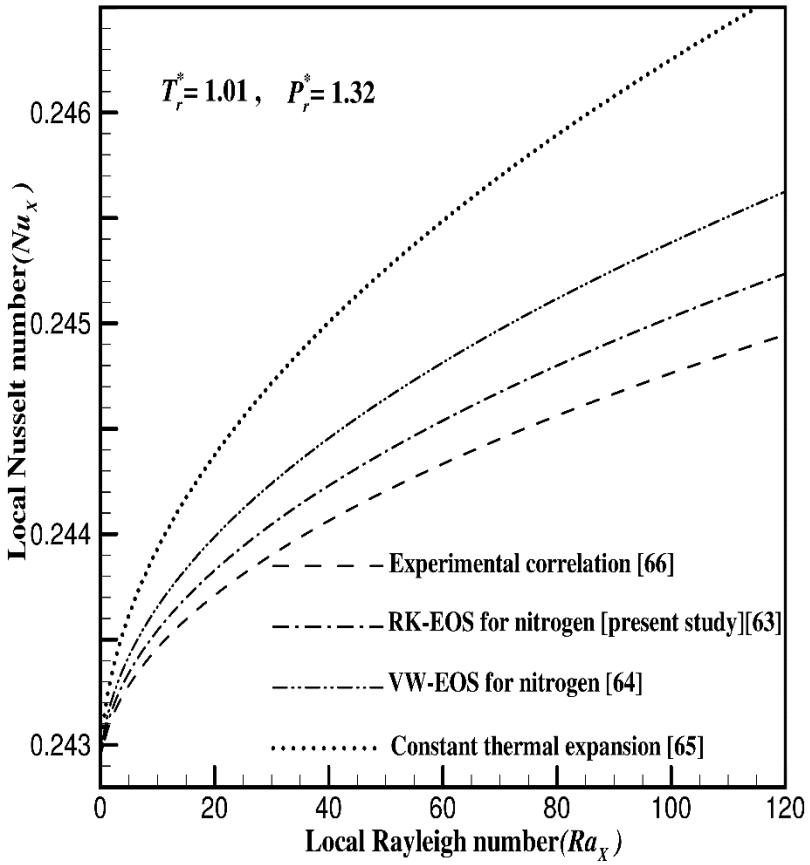

Fig. 5. Nu_X as a function of Ra_X for nitrogen at $T_r^* = 1.01$ and $P_r^* = 1.32$ based on experimental correlation [66], RK-EOS [63], VW-EOS [64] with ideal gas [65].

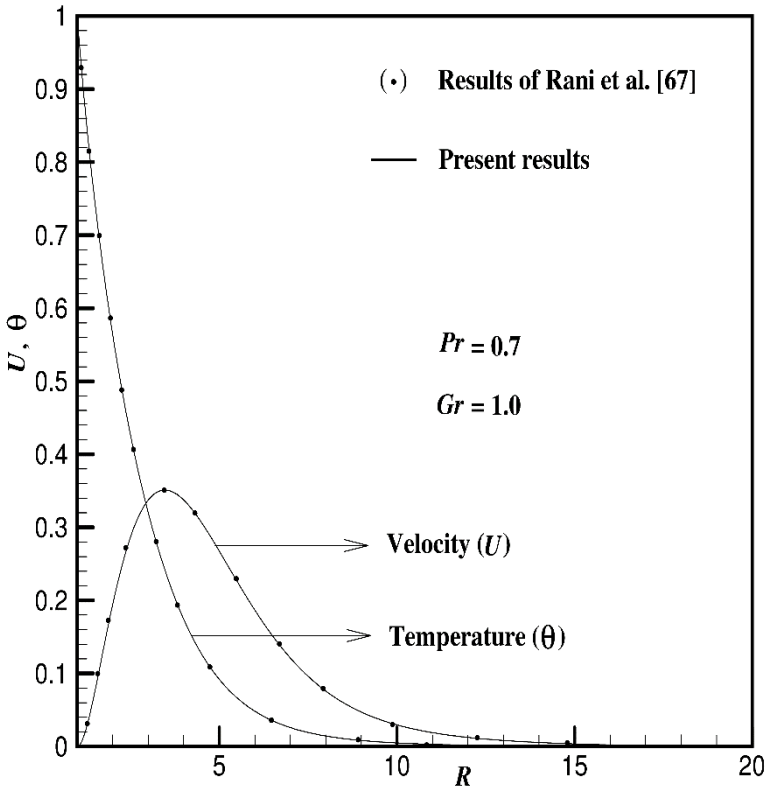

Fig. 6. Comparison of present results with available existing results [67].

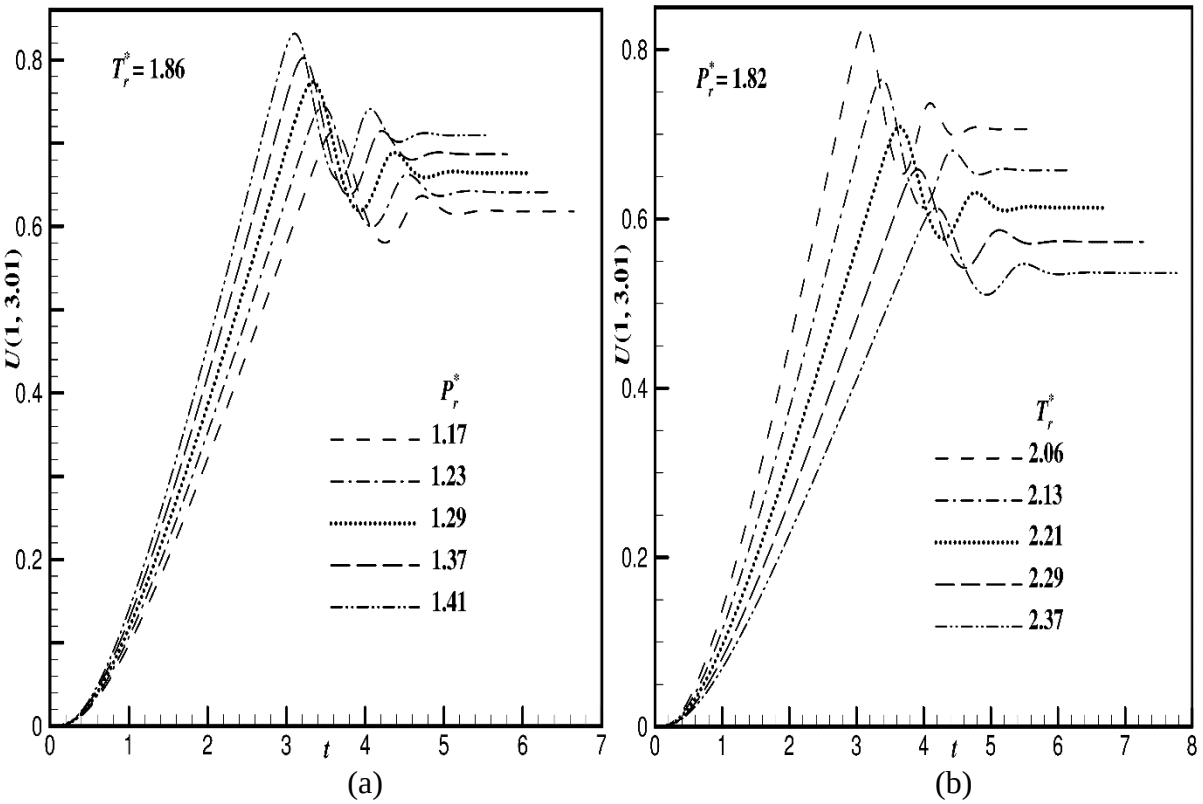

Fig. 7. Transient velocity profile (U) at (1, 3.01) versus time (t) for various values of (a) P_r^* and (b) T_r^*.

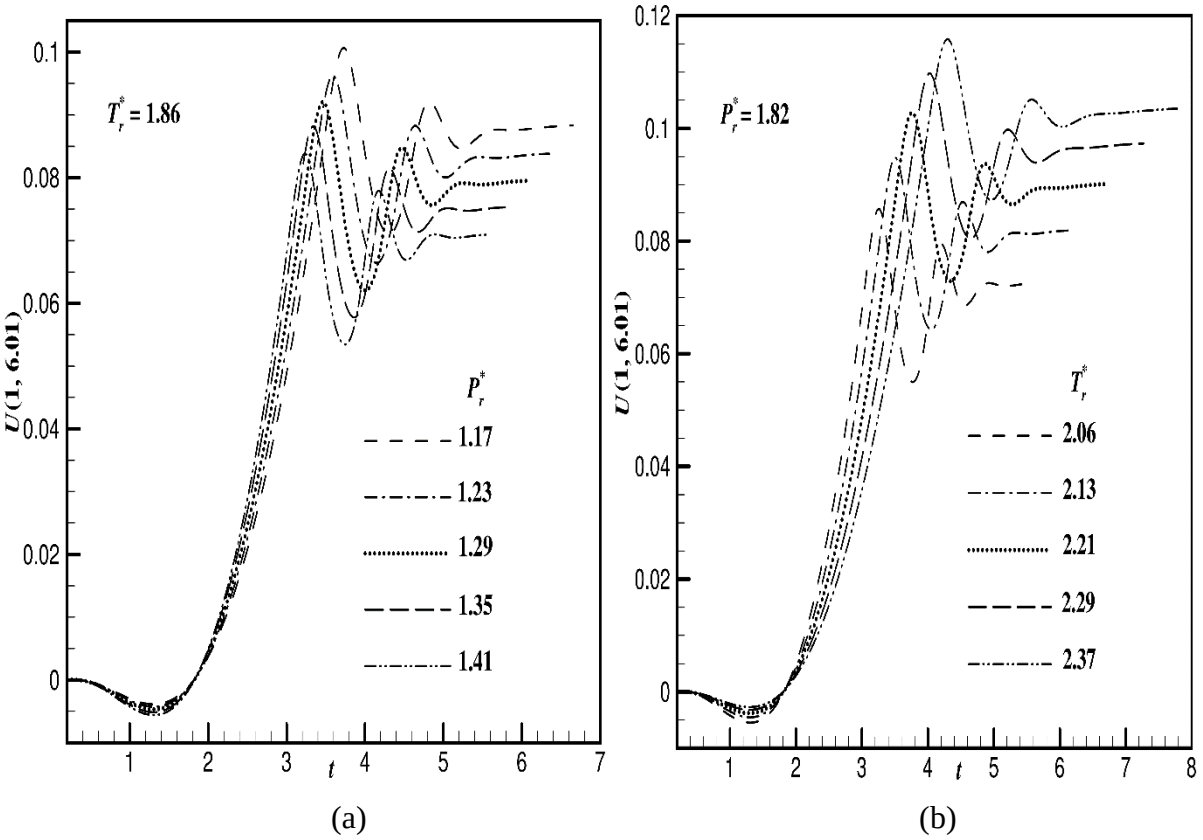

Fig. 8. Transient velocity profile (U) at the location (1, 6.01) versus time (t) for various values of (a) P_r^* and (b) T_r^*.

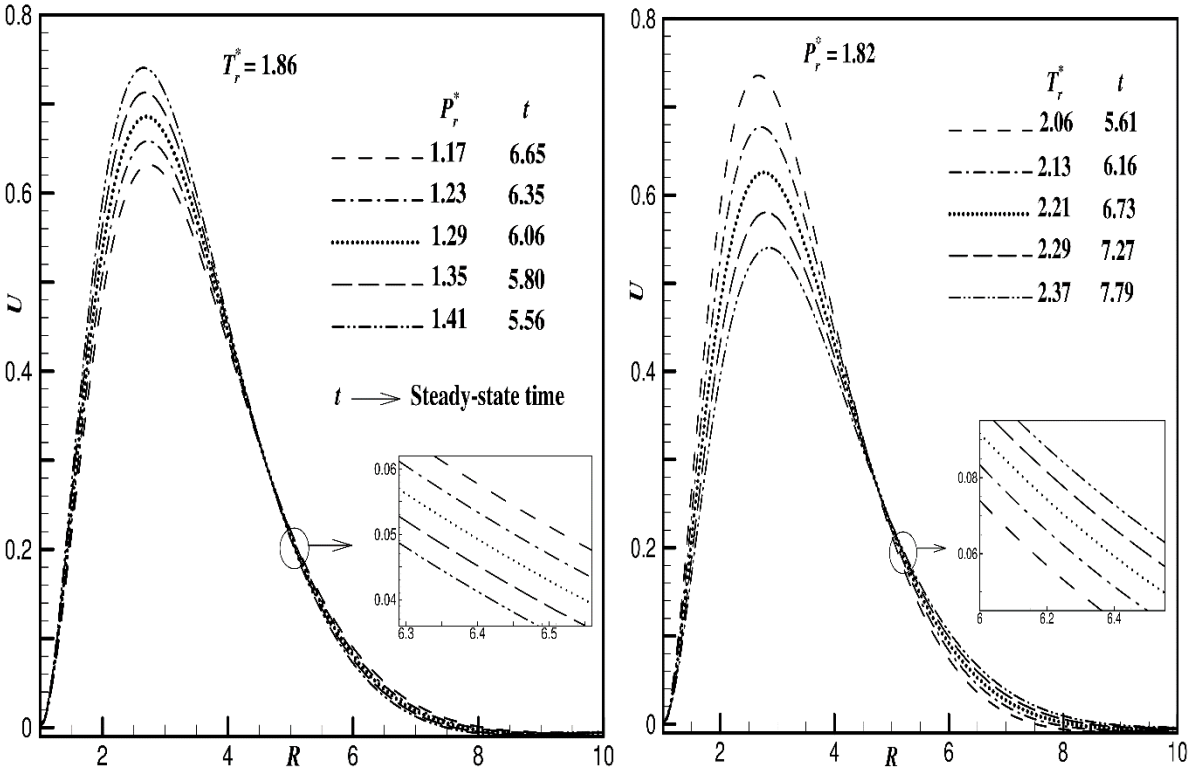

(a) (b)

Fig. 9. Steady-state velocity profile (U) versus R at $X = 1.0$ for various values of (a) P_r^* and (b) T_r^*.

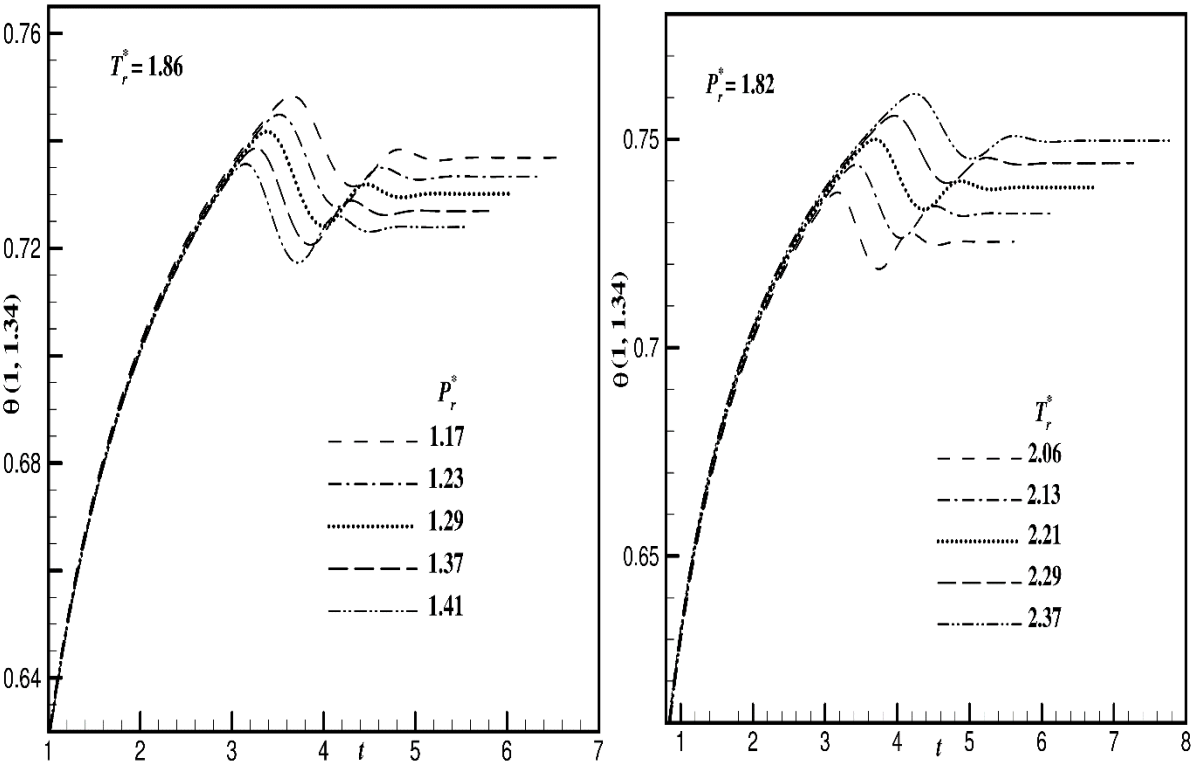

(a) (b)

Fig. 10. Transient temperature profile (θ) at (1, 1.34) versus time (t)for different values of (a) $P_r^*$and (b) T_r^*.

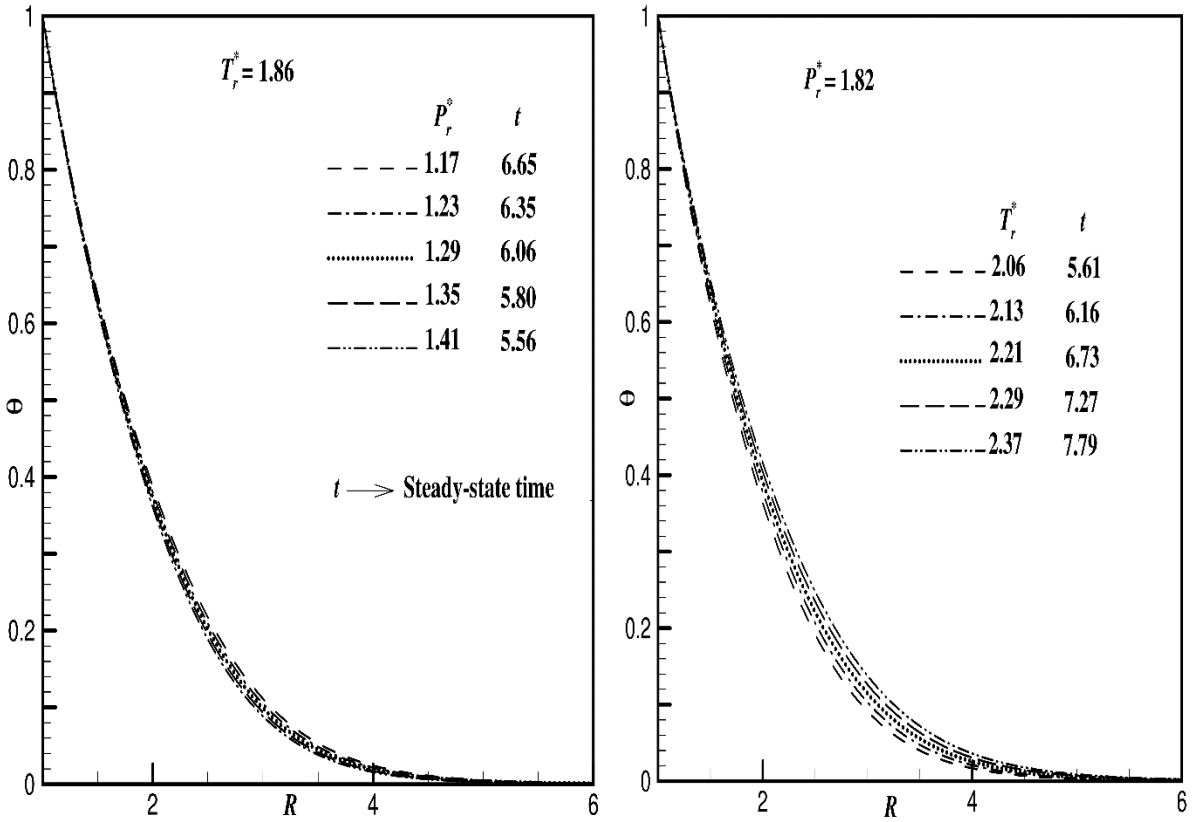

(a) (b)

Fig. 11. Steady-state temperature profile (θ) versus Yat $X = 1.0$ for various values of (a) P_r^* and (b) T_r^*.

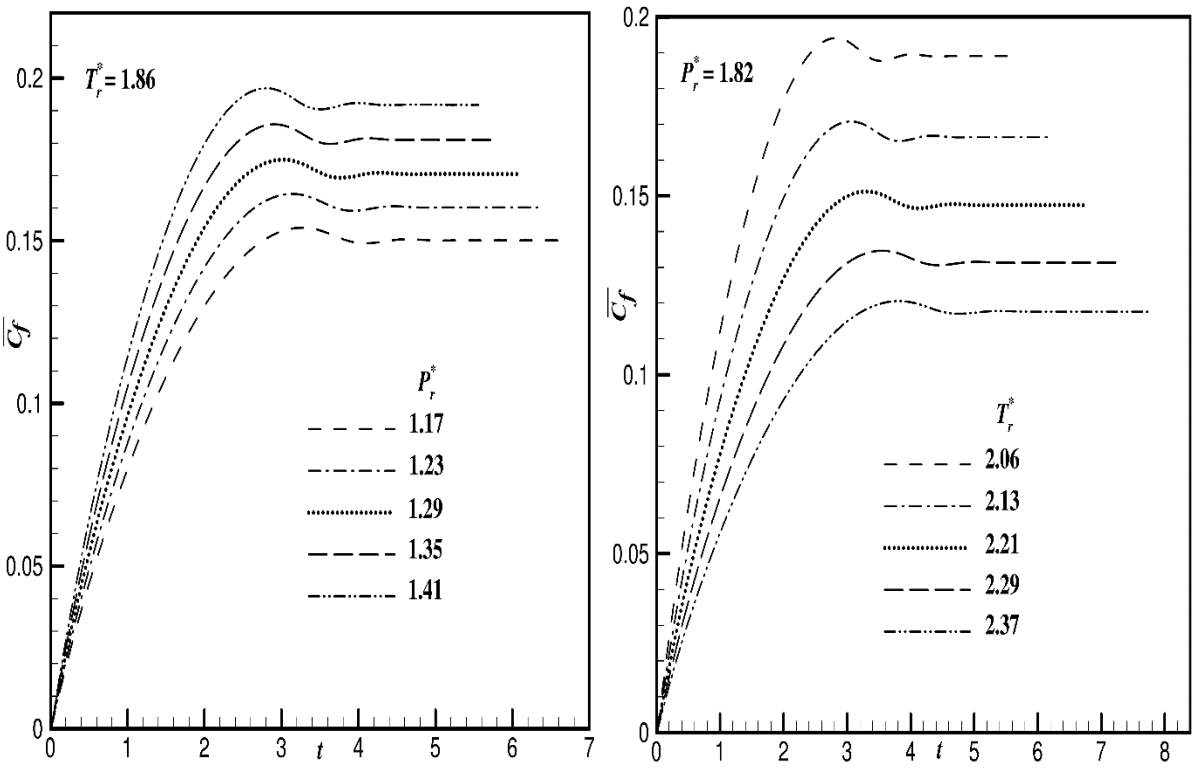

(a) (b)

Fig. 12. Average skin-friction coefficient ($\overline{C_f}$) for various values of (a) P_r^*, (b) T_r^*.

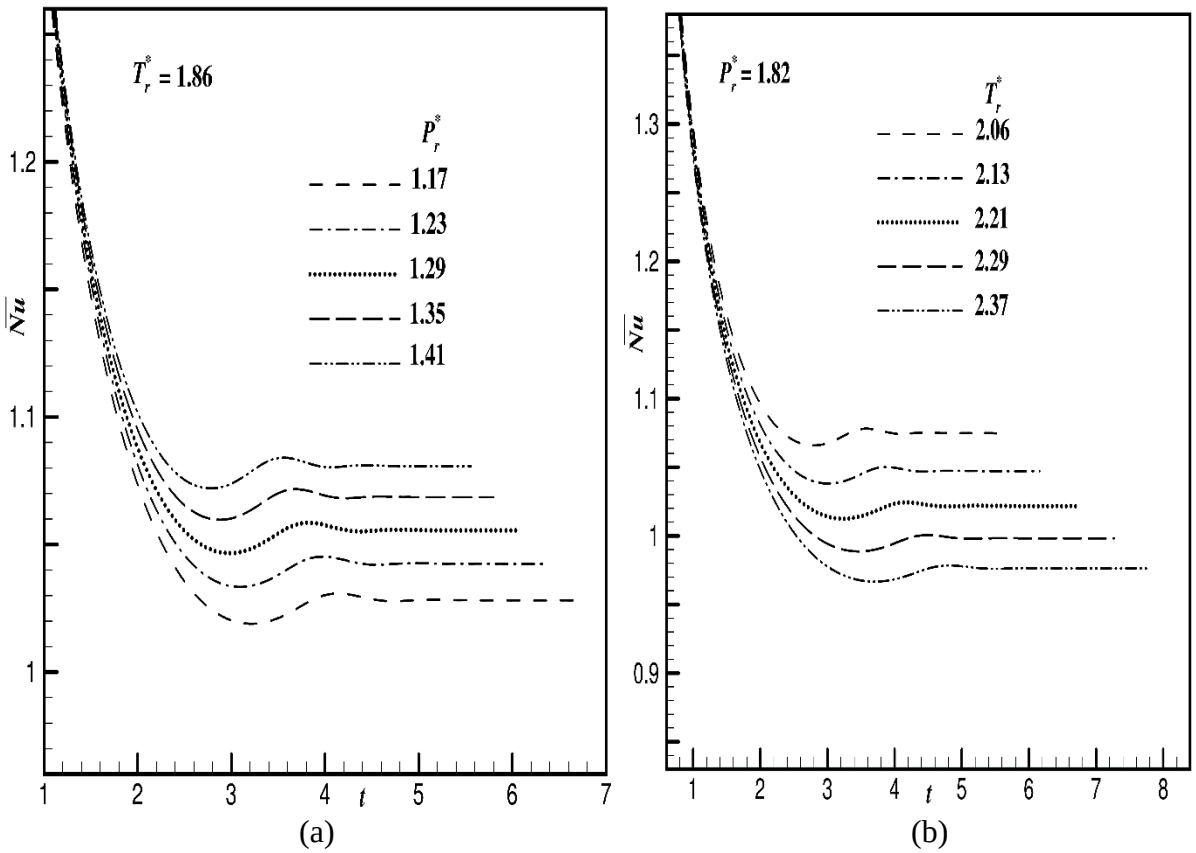

(a) (b)

Fig. 13. Average Nusselt number ($\overline{Nu}$) for various values of (a) P_r^*, (b) T_r^*.

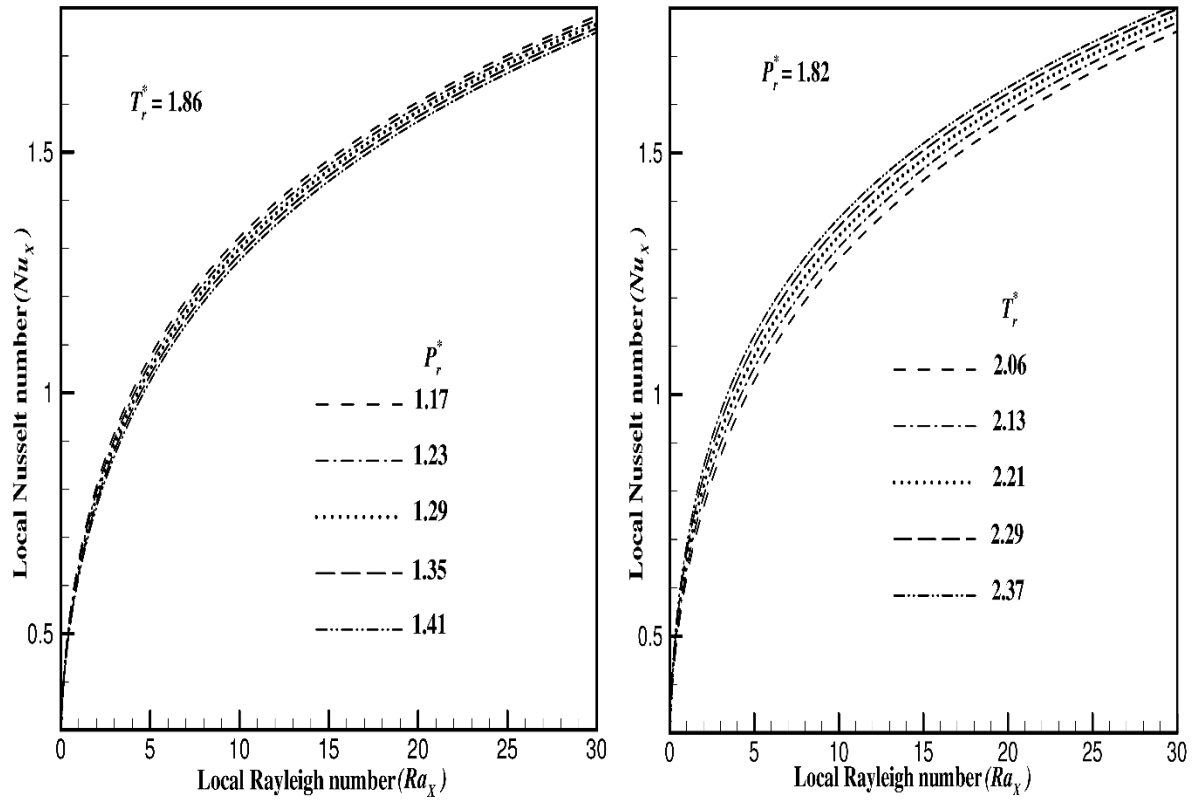

(a) (b)

Fig. 14. Local Nusselt number (Nu_X) as a function of local Rayleigh number (Ra_X) for nitrogen at (a) fixed T_r^* and various values of P_r^*; (b) fixed P_r^* and various values of T_r^*.

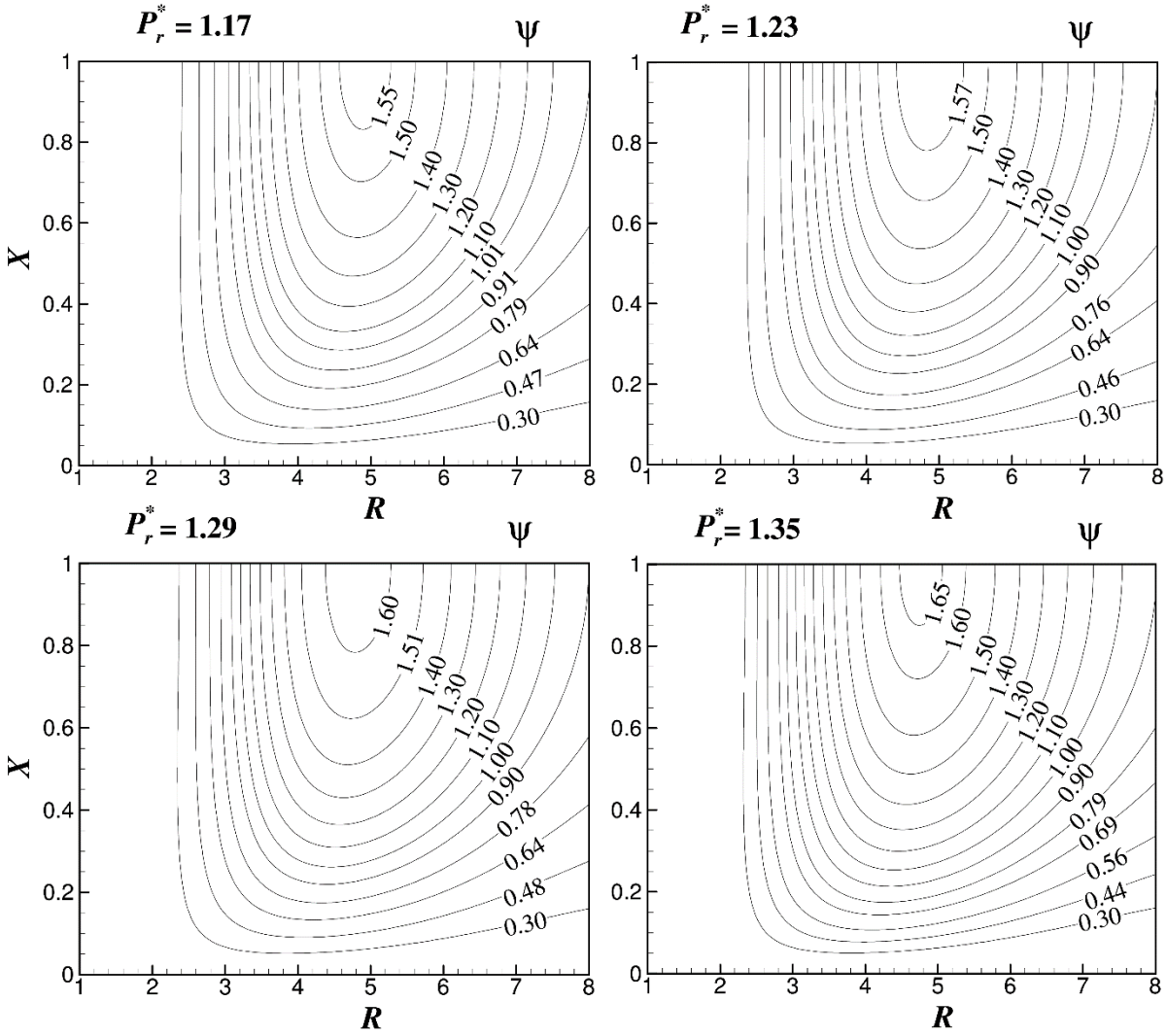
$P_r^* = 1.17$
ψ
1.55
1.50
1.40
1.30
1.20
1.10
1.01
0.91
0.79
0.64
0.47
0.30
$P_r^* = 1.23$
ψ
1.57
1.50
1.40
1.30
1.20
1.10
1.00
0.90
0.76
0.64
0.46
0.30
$P_r^* = 1.29$
ψ
1.60
1.51
1.40
1.30
1.20
1.10
1.00
0.90
0.78
0.64
0.48
0.30
$P_r^* = 1.35$
ψ
1.65
1.60
1.50
1.40
1.30
1.20
1.10
1.00
0.90
0.79
0.69
0.56
0.44
0.30
X
R

15 (a)

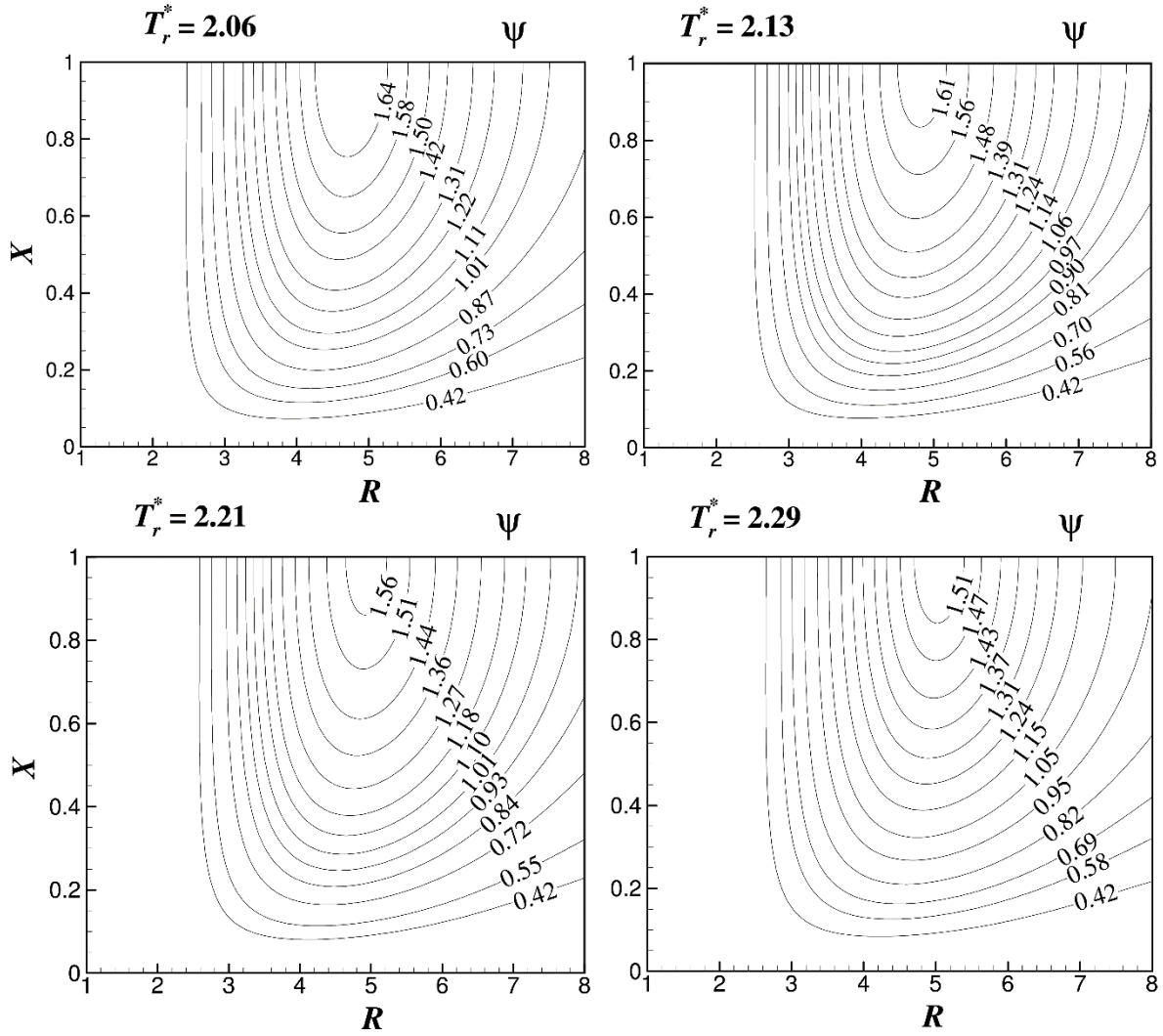

15 (b)

Fig. 15. Streamlines (ψ) for various values of (a) P_r^* and (b) T_r^*.

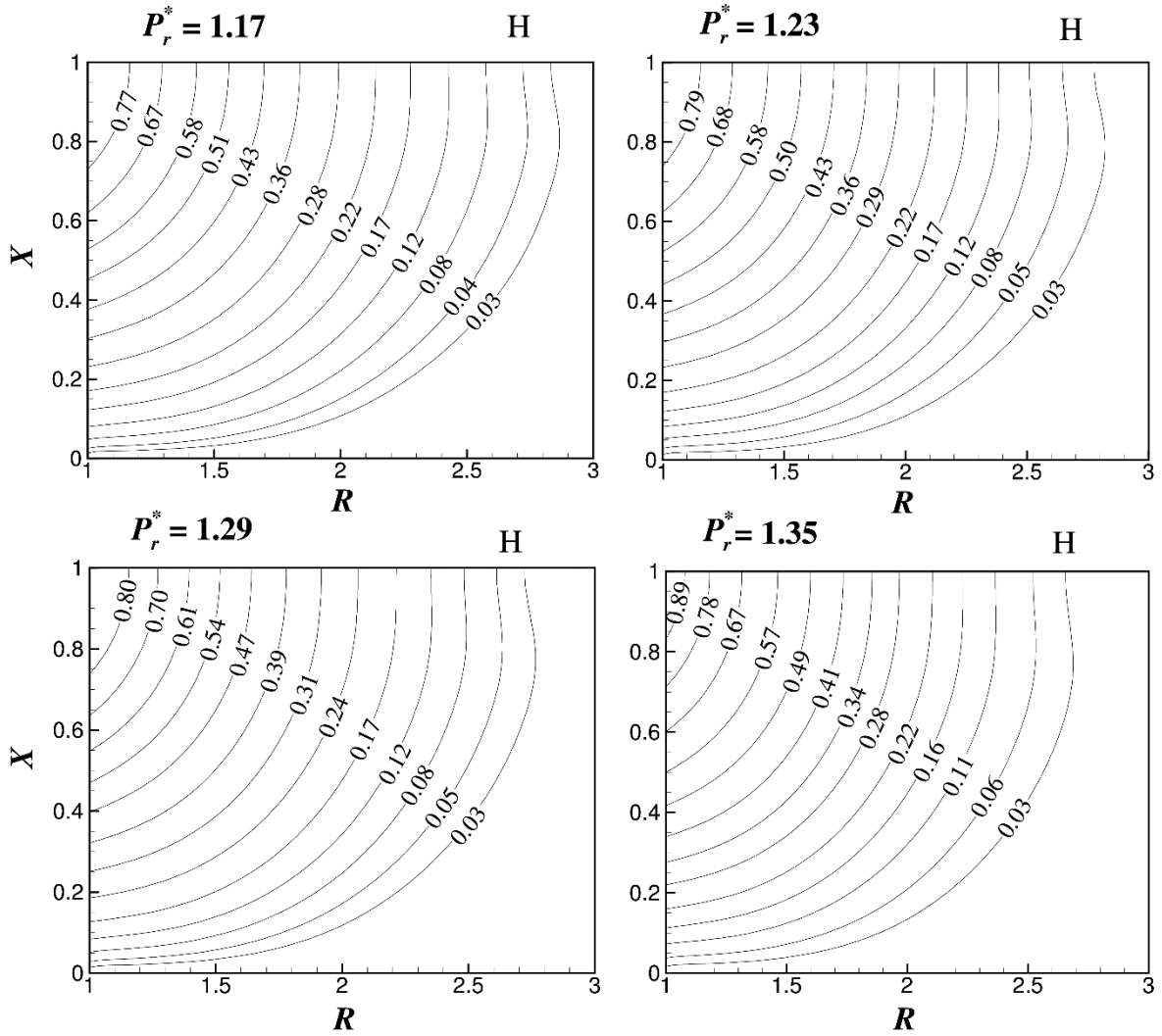
$P_r^* = 1.17$
H
0.77
0.67
0.58
0.51
0.43
0.36
0.28
0.22
0.17
0.12
0.08
0.04
0.03
$P_r^* = 1.23$
H
0.79
0.68
0.58
0.50
0.43
0.36
0.29
0.22
0.17
0.12
0.08
0.05
0.03
$P_r^* = 1.29$
H
0.80
0.70
0.61
0.54
0.47
0.39
0.31
0.24
0.17
0.12
0.08
0.05
0.03
$P_r^* = 1.35$
H
0.89
0.78
0.67
0.57
0.49
0.41
0.34
0.28
0.22
0.16
0.11
0.06
0.03
X
R
0
0.2
0.4
0.6
0.8
1
1
1.5
2
2.5
3

16 (a)

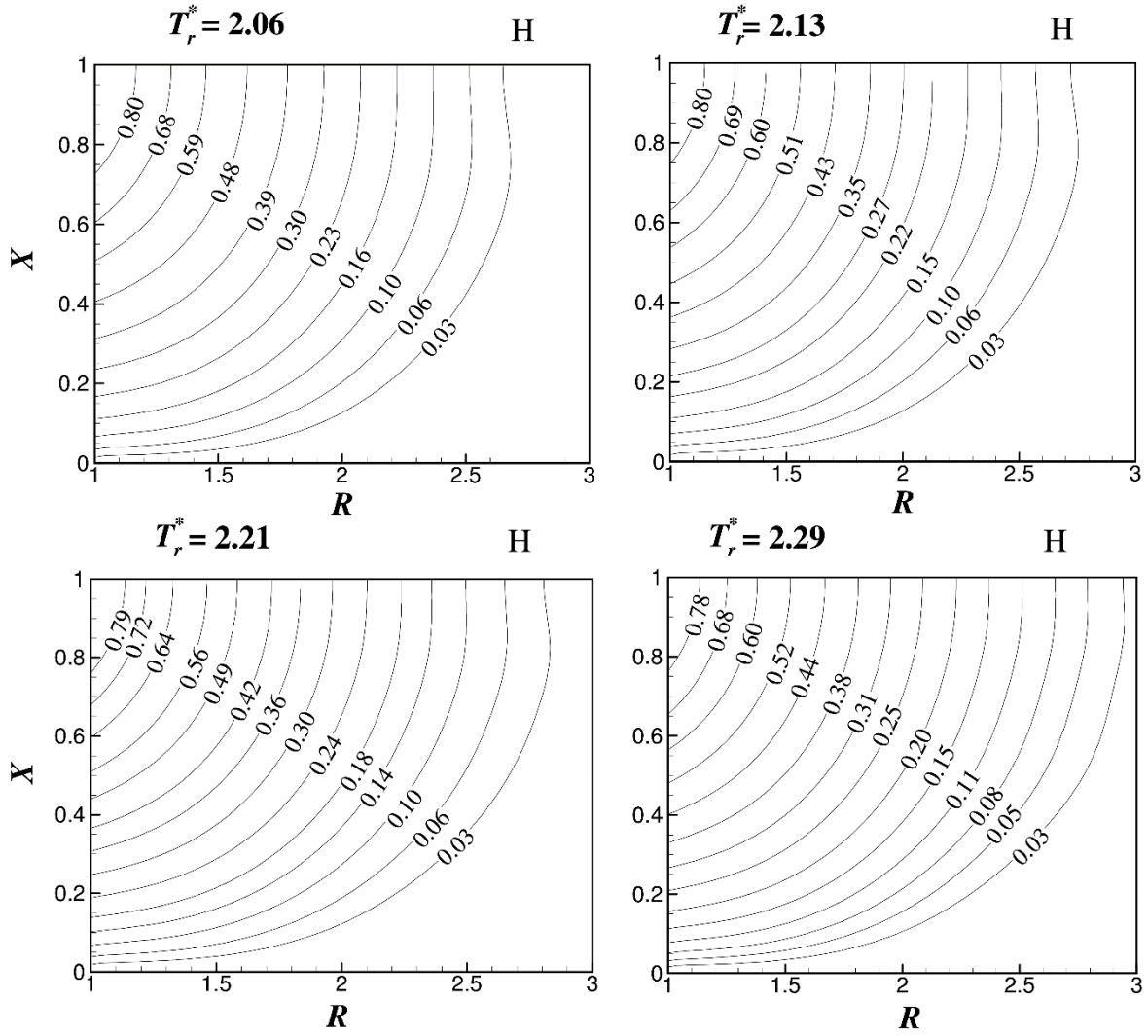

16 (b)

Fig. 16. Heatlines (H) for various values of (a) P_r^* and (b) T_r^*.

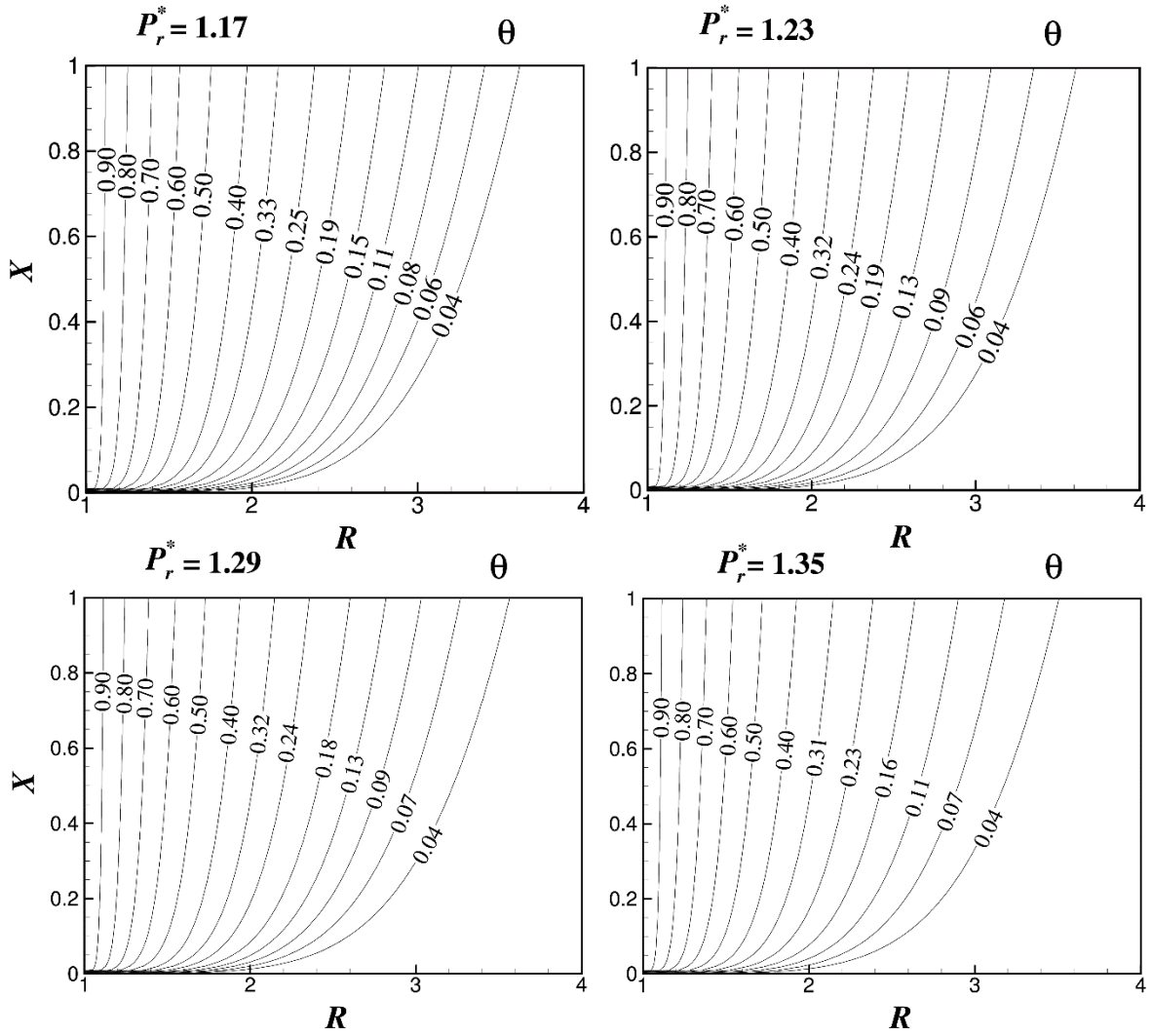
$P_r^* = 1.17$
θ
0.90
0.80
0.70
0.60
0.50
0.40
0.33
0.25
0.19
0.15
0.11
0.08
0.06
0.04
$P_r^* = 1.23$
θ
0.90
0.80
0.70
0.60
0.50
0.40
0.32
0.24
0.19
0.13
0.09
0.06
0.04
$P_r^* = 1.29$
θ
0.90
0.80
0.70
0.60
0.50
0.40
0.32
0.24
0.18
0.13
0.09
0.07
0.04
$P_r^* = 1.35$
θ
0.90
0.80
0.70
0.60
0.50
0.40
0.31
0.23
0.16
0.11
0.07
0.04
X
R

17(a)

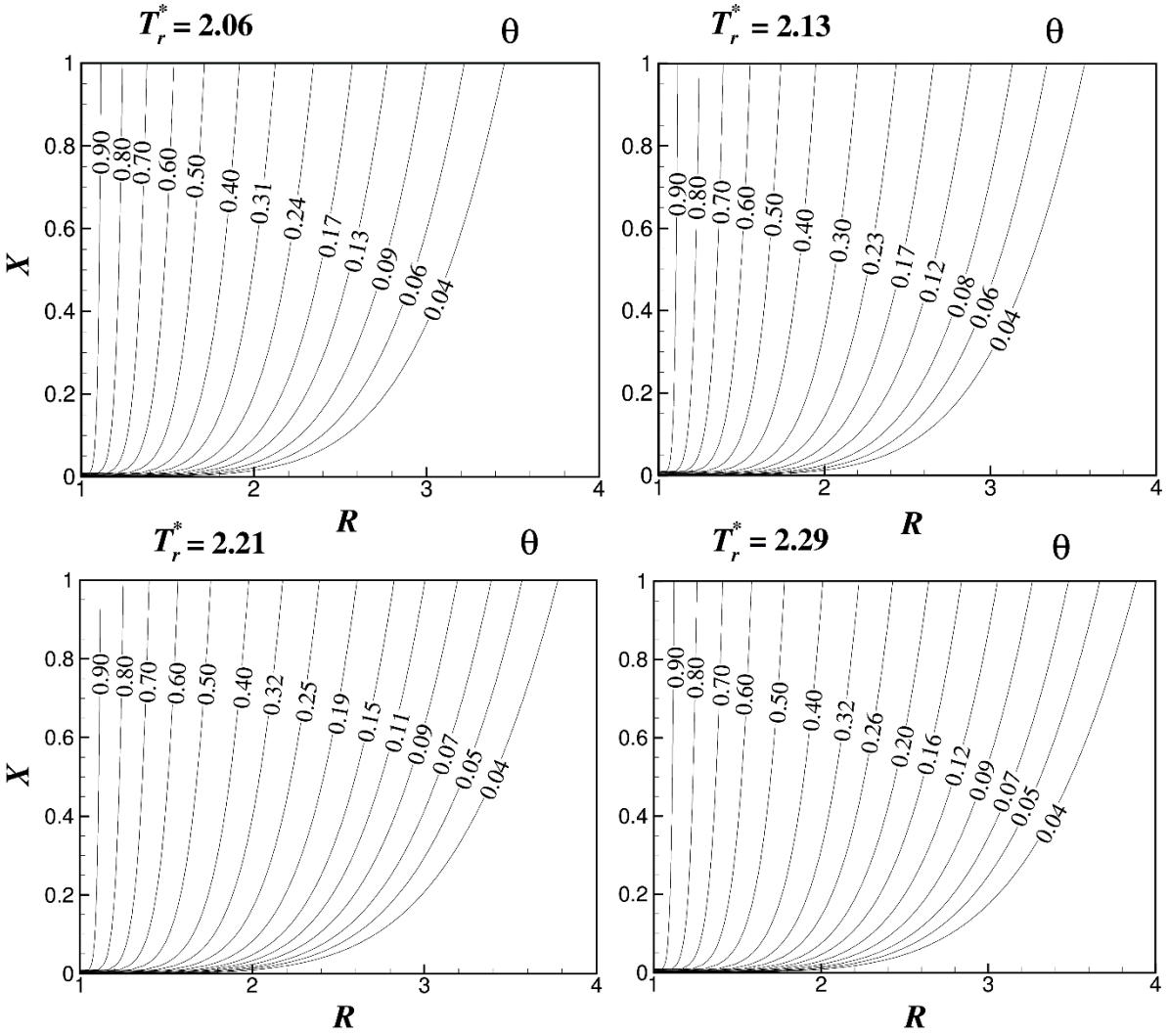

17 (b)

Fig. 17. Isotherms (θ) for various values of (a) P_r^* and (b) T_r^*.